FAN NOISE ATTENUATION WITH AN ACOUSTIC METAMATERIAL

by

Ryan Hill

A dissertation submitted to the faculty of
The University of North Carolina at Charlotte
in partial fulfillment of the requirements
for the degree of Master of Science in
Electrical Engineering

Charlotte

2021

Approved by:

_____

Dr. Ed Stokes

_____

Dr. Thomas Weldon

_____

Dr. Kathryn Smith

ABSTRACT

RYAN HILL. Fan Noise Attenuation with an Acoustic Metamaterial. (Under the direction of DR. ED STOKES)

In a world continuously increasing in the number of electronic devices, the need for cooling fans increases and so does its contribution to noise pollution. This project explores a solution to this problem by designing an acoustic metamaterial that attenuates the fan noise from a Sofasco fan, whose fundamental blade pass frequency is approximately 800 Hz. According to Ping, two Helmholtz resonators (HRs) that are parallel side branched to a waveguide whose distance is less than a wavelength will have a hybrid resonance at the difference average. This approach did not work with the first generation samples, but the use of two parallel HRs was used in future designs. According to Sang-Hyun, the attenuation increases logarithmically for each parallel HR side branched to a waveguide. Using Sang-Hyun method, a second generation sample was designed that achieved a transmission loss of 45 dB, but it had an airflow loss of 75%. Other second generation designs explored decreasing the airflow loss, but none of the methods were successful. The third generation design has a waveguide shaped as a truncated sector, which increases the cross-sectional area of the waveguide as well as the airflow. The best sample of the third generation design had a transmission loss of 30 dB with an airflow loss of 45%. In an attempt to further decrease the airflow loss, the fourth generation design placed two HRs connected in series with each other (dual HRs) a side branch to the waveguide. The airflow loss was reduced to less than 1% with transmission loss of approximately 18 dB at 496 Hz and 1250 Hz. This design also led to a transmission loss of approximately 8 dB from 582 Hz to 1000 Hz. This design was never modified to achieve the fan frequency of 800 Hz, but this can be achieved using design equations for dual HRs.

DEDICATION

I would like to dedicate this work to my parents, Jimmy & Jane Hill, and my brother, Matthew Hill, for all the support they gave while perusing my dream. In addition, I would like to dedicate this work to my fiancee, Heather Gwyn, for her constant support.

ACKNOWLEDGEMENTS

I would like to acknowledge my advisor, Dr. Ed Stokes, for his guidance, advice, and knowledge, which helped me in the successful design of an acoustic metamaterial. I would like to acknowledge, Dr. Thomas Weldon, for introducing me to the concept of metamaterials and continuing to be a source of knowledge for me.

I would like to acknowledge the Center for Metamaterials and the National Science Foundation for their funding, which allowed me to complete this work. The Harris Corporation and Riverside Research, which are part of the Center for Metamaterials, provided invaluable support and feedback for our project.

I would like to acknowledge the Electrical & Computer Engineering department and the Harris Corporation, for their financial support in buying the anechoic chamber, the audio analyzer, and the impedance tube. My thesis would not be possible without this equipment.

Finally, I would like to acknowledge Matias Menndieta and Patrick Bruce for their work as undergraduate researchers on the project, where they helped in every aspect of the project.

TABLE OF CONTENTS

LIST OF TABLES ix

LIST OF FIGURES x

LIST OF ABBREVIATIONS xiv

CHAPTER 1: INTRODUCTION 1

1.1. Theory 1

1.1.1. Volumetric Mass Density 1

1.1.2. Stress 2

1.1.3. Strain 3

1.1.4. Bulk Modulus 4

1.1.5. Speed of Sound 5

1.1.6. Pressure 6

1.1.7. Particle Velocity 8

1.1.8. Volume Velocity 9

1.1.9. Impedance 9

1.1.10. Intensity 10

1.1.11. Sound Intensity Level & Sound Pressure Level 10

1.1.12. Q-factor 11

1.1.13. Capacitor 12

1.1.14. Inductor 13

1.1.15. Resonators 13

1.1.16. Continuity Equation 17

1.1.17. Bernoulli's Equation 17

1.1.18. Brake Horsepower 18

1.1.19. Fan Affinity Laws 19

1.1.20. Fan Noise 20

1.1.21. Metamaterials 22

1.2. Literature Review 23

1.2.1. Silencer design by using array resonators for low-frequency band noise reduction 24

1.2.2. Redesigning Helmholtz resonators to achieve attenuation at multiple frequencies 25

1.2.3. Benchmark Analysis of a Helmholtz Resonator for Estimating Acoustic Metamaterial Properties 26

1.3. Fan Characteristics 30

1.4. Introduction to Design 35

CHAPTER 2: EXPERIMENTS & RESULTS: LARGE SCALE EXPERIMENTS 37

2.1. Experimental Setup 39

2.2. Experiment: Single HR With No Flow 40

2.3. Experiment: Single HR As A Side Branch With No Flow 41

2.4. Experiment: Two Parallel HR As Side Branches With No Flow 43

CHAPTER 3: SAMPLES AND SAMPLE EXPERIMENTS 45

3.1. Experimental Setup & Hardware 46

3.1.1. Impedance Tubes & Transmission Loss Measurements 46

3.1.2. Insertion Loss Measurements 49

3.1.3. Airflow Measurement Setup 51

3.2. Samples 52

3.2.1. Sample S1_1 53

3.2.2. Second Generation Sample Design 56

3.2.3. Sample: S2_1_Blank 58

3.2.4. Sample: S2_1 60

3.2.5. Sample: S2_1_SF 65

3.2.6. Sample: S2_1_DF 67

3.2.7. Sample: S2_2 69

3.2.8. Third Generation Sample Design 71

3.2.9. Sample: S3_1 73

3.2.10. Sample: S3_3 76

CHAPTER 4: CONCLUSIONS 79

REFERENCES 84

LIST OF TABLES

TABLE 1.1: The table list properties of the Sofasco cooling fan [1]. 31

TABLE 1.2: The table lists the first 5 harmonics of the fan's BPF and SBRF. 32

TABLE 1.3: The table lists the first 5 harmonics of the fan's BPF and SBRF. 34

TABLE 1.4: The table lists the fan's BPF with varying operating voltages. 35

TABLE 2.1: The table contains the physical dimensions of the Thermofisher Scientific 50 mL volumetric flask, where some of the dimensions were measured in the lab. 38

TABLE 2.2: The resonance frequencies of a single resonator with varied volume for both the physical and simulated experiments. 40

TABLE 2.3: The resonance frequencies of a single resonator that is a side branch with varied cavity volumes. 42

TABLE 2.4: The resonance frequencies of a single resonator that is a side branch with varied cavity volumes. 44

TABLE 3.1: Resonance Frequencies for Sample S2_1 62

TABLE 3.2: The surface areas and volumes of the resonators for the original design and the adjusted design. 70

LIST OF FIGURES

FIGURE 1.1: The figure illustrates a visual example of a substance's modulus of elasticity or bulk modulus. 4

FIGURE 1.2: The figure shows an example of pressure with a normal force applied over a unit area. 6

FIGURE 1.3: The figure shows an example of volume velocity. 9

FIGURE 1.4: The quality factor of a resonance peak as shown in [2]. 11

FIGURE 1.5: The figure shows various types of Helmholtz resonators as shown in [2]. 14

FIGURE 1.6: The figure shows the equivalent RLC circuit of a HR as shown in [2]. 15

FIGURE 1.7: The figure shows an example of when Bernoulli's equation would be used. 17

FIGURE 1.8: The figure displays the internals parts of a computer fan motor and the red arrow identifies the fan's sleeve bearing. 20

FIGURE 1.9: The figure shows a graph with the classification of acoustic metamaterials by the value of mass density and bulk modulus. The graph was taken from [3]. 23

FIGURE 1.10: The figure as shown in the paper, shows how the author defined different volumes in the HR's cavity. 25

FIGURE 1.11: The figure shows the metamaterial unit cells explored in the article. The first image shows a unit cell with a single HR and the second image shows a unit cell made of two series HRs. The unit cells were connected to the impedance tube where the sample holder is normally placed. 26

FIGURE 1.12: The figure is a drawing of the CAD model for a Sofasco D6025V12SHBL-03 fan with the fan's dimensions, which was provided by the manufacturer online. 30

FIGURE 1.13: In the frequency domain, the figure shows the SPL of the fan at operating voltage (12V). 33

FIGURE 1.14: In the frequency domain, the figure shows the SPL of the fan's BPF for varying operating voltages. 34

FIGURE 2.1: The volumetric flask used as a HR for the experiments conducted in the lab. 37

FIGURE 2.2: The figure is a flow chart of the experimental setup for any large scale experiment. 39

FIGURE 2.3: The physical setup for the single resonator experiment. 40

FIGURE 2.4: The physical setup of the Helmholtz resonator acting as a side branch for the insertion loss measurement. This pipe is positioned in the anechoic chamber for the measurement. 41

FIGURE 2.5: The physical results for the insertion loss of a single resonator that is a side branch with varied cavity volumes. 42

FIGURE 2.6: The physical experimental setup for the insertion loss experiment of two parallel HRs acting as side branches. 43

FIGURE 2.7: The measured results of the difference in SPL for the two parallel HRs acting as a side branch. 44

FIGURE 3.1: The figure is the two impedance tubes that are used in the acoustics lab. 46

FIGURE 3.2: The figure shows the flowchart for the transmission loss measurement and absorption measurement using the equipment in the lab. 47

FIGURE 3.3: The transmission loss of the empty impedance tube. 49

FIGURE 3.4: The figure shows the setup for insertion loss measurements using the impedance tube. 51

FIGURE 3.5: The first setup for the airflow experiments. 52

FIGURE 3.6: The figure shows the setup used for the airflow experiment. 52

FIGURE 3.7: The figure shows the evolution of the samples, which are the different design branches. 53

FIGURE 3.8: The figure shows the layout of the HRs as shown in Peng and Sheng's paper on metamaterials[4]. 54

FIGURE 3.9: The figure shows the unit cells that make up sample: S1_1 as well as sample: S1_1. 54

FIGURE 3.10: The figure shows the insertion loss for sample: S1_1. 55

FIGURE 3.11: The figure shows the base design for all second generation designs, where the sample has a upper (outer) resonator, a lower (inner), and a center (middle) resonator. 57

FIGURE 3.12: The figure shows the inside of a 3D printed second generation sample using a five dollar bill as a reference. 57

FIGURE 3.13: The CAD design of the S2_1_Blank sample. 58

FIGURE 3.14: The transmission loss of the sample S2_1_Blank from 250 Hz to 1600 Hz. 59

FIGURE 3.15: The transmission loss of the S2_1_Blank sample from the COMSOL simulations. 60

FIGURE 3.16: The CAD design of sample S2_1. 60

FIGURE 3.17: The measured transmission loss of the sample S2_1. 61

FIGURE 3.18: The results of the COMSOL simulation for sample S2_1. 62

FIGURE 3.19: The transmission loss of sample S2_1 from 250 Hz to 1600 Hz at different orientations. 63

FIGURE 3.20: The measured insertion loss of the sample S2_1 from 0 Hz to 1100 Hz. 64

FIGURE 3.21: The airflow and airflow loss of the sample S2_1. 65

FIGURE 3.22: The CAD design of sample S2_1_SF. 65

FIGURE 3.23: The airflow and airflow loss of the sample S2_1_SF. 66

FIGURE 3.24: The transmission loss of the sample S2_1_SF from 250 Hz to 1600 Hz for different orientations. 66

FIGURE 3.25: The CAD design of sample S2_1_DF. 67

FIGURE 3.26: The transmission loss of the sample S2_1_DF from 250 Hz to 1600 Hz. 68

FIGURE 3.27: The airflow and airflow loss of the sample S2_1_DF. 68

FIGURE 3.28: The CAD design for sample S2_2. 69

FIGURE 3.29: The transmission loss of sample S2_2 from 250 Hz to 1600 Hz. 71

FIGURE 3.30: The figure is a cross sectional piece of the base design for the third generation samples. The waveguide is the truncated sector that is highlighted in blue. 72

FIGURE 3.31: The CAD design for sample S3_1. 73

FIGURE 3.32: The airflow and airflow loss of sample S3_1. 74

FIGURE 3.33: The measured transmission loss of sample S3_1 from 250 Hz to 1600 Hz, with a resonance at 790 Hz. 75

FIGURE 3.34: The CAD design for sample S3_3. The red arrow indicates how the waveguide's surface area will increase. The green arrows show how the resonators' surface area will decrease. 76

FIGURE 3.35: The measured transmission loss of sample S3_3 from 250 Hz to 1600 Hz, with a resonance at 800 Hz. 77

FIGURE 3.36: The airflow and airflow loss of the sample S3_3. 78

FIGURE 4.1: The first broadband design for an acoustic metamaterial. 81

FIGURE 4.2: The second broadband design for an acoustic metamaterial. 81

LIST OF ABBREVIATIONS

BHP	An abbreviation for brake horsepower.
BPF	An abbreviation for Blade Pass Frequency.
CAD	An abbreviation for Computer-aided Design.
dB	An abbreviation for Decibel.
ECE	An acronym for Electrical and Computer Engineering.
hp	An abbreviation for horsepower, which is unit of power.
HR	An abbreviation for Helmholtz Resonator.
Hz	An abbreviation for Hertz.
IL	An abbreviation for Insertion Loss.
Pa	An abbreviation for Pascal.
QF	An abbreviation for Quality Factor
RPM	An abbreviation for Revolutions Per Minute.
SBRF	An abbreviation for Sleeve Bearing Rotation Frequency.
SI	An abbreviation for International System.
SM	An abbreviation for Scattering Matrix.
SPL	An abbreviation for Sound Pressure Level.
TL	An abbreviation for Transmission Loss.
TM	An abbreviation for Transfer Matrix.

CHAPTER 1: INTRODUCTION

The research team had the task of attenuating the noise created from a Sofasco D6025V12SH-03 computer fan using an acoustic metamaterial, while limiting the restrictions to air flow. The specifications of the Sofasco fan is found in table 1.1 and in the data sheet for the Sofasco fan [1].

This chapter is split into the four sections consisting of the theory section, the literature review section, the fan characteristics section and the design section. The section of the fan characteristics introduces the properties of the Sofasco fan, including the its' noise spectrum and the noise producing mechanisms. In the literature review section, the articles and papers that contained theory and concepts useful in the design process. The theory section, which contains multiple subsections, introduces and reviews important concepts in the fields of acoustics, thermodynamics, and fluid dynamics. The final section of the chapter introduces the basic design techniques that will be used to design and fabricate the acoustic metamaterial.

1.1 Theory

In this section, the relevant theory needed to understand topics in later sections and chapters is introduced. This section starts with the definition of mass density and expands on topics required to defined the speed of sound and pressure. The definition of different types of velocity is explored and shows the relationship to impedance. In addition, topics explaining the nature of airflow are explored later in the section.

1.1.1 Volumetric Mass Density

The volumetric mass density, or mass density, of a material is generally defined as mass per unit volume, where the SI units are given as kg/m^3. In a homogeneous

material, the density can be defined as:

$$\rho = \frac{m}{v} \quad \left[\frac{kg}{m^3}\right] \tag{1.1}$$

where m is the mass in kg and v is the volume in m^3 [5]. However, most materials are heterogeneous and therefore, the density is locally defined as:

$$\rho\,(\overrightarrow{r}) = \frac{dm}{dv} \quad \left[\frac{kg}{m^3}\right] \tag{1.2}$$

where dm is an infinitesimal mass in kg, dv is an infinitesimal volume in m^3, and r is the location of the infinitesimal volume.

1.1.2 Stress

A load is a force that is applied to the surface or body of a material. An external load on a body creates internal forces, which are forces applied between particles inside a body. Stress is the internal forces per area that act as a restoring force to the external load applied to a body or surface [6]. Mathematically, stress is defined as the force per unit area and it is given by:

$$\sigma = \frac{F}{A} \quad \left[\frac{N}{m^2}\right] \tag{1.3}$$

where F is the force in newtons and A is the surface area that the force is applied over in m^2 [6]. For more complicated systems or systems that are not in the linear region, stress is generally defined with a stress tensor. The units of stress are given as units of pressure that is in units of pascal. However, stress is not the same as pressure and this can be easily shown with the tensor representation of stress [7, 8]. The two main types of stress are normal stress and shear stress, which differ only in the direction the external load is applied.

1.1.2.1 Normal Stress

Normal stress, or direct stress, is the internal forces that act as a restoring force to the external load applied normal to the surface(s) of a body [6]. It can be further categorized as either a longitudinal stress or volumetric stress [6]. Longitudinal stress occurs from equal and opposite external loads that are applied to surfaces on two opposing sides of a body, which causes deforming along the length of the body [6]. Longitudinal stress can be further classified as either tensile stress or compressive stress depending on the body's deformed length. Volumetric stress, or bulk stress, occurs from external loads applied over every surface of a body, which can cause deforming to occur [6].

1.1.2.2 Shear Stress

Shear stress is defined as a force applied parallel or across the surface [6]. An example of shearing stress is when one metal plate is slide across another stationary plate.

1.1.3 Strain

Strain is defined, generally, as the unit-less measure of a body's deformation due to the load(s) applied to the body [8]. There are different types of strains, that are classified based on how and where the load is applied to the body. The mathematical definition of strain in complex systems is defined using strain tensors, but it can be used to define strain for any system.

1.1.3.1 Direct Strain

Direct strain, or linear strain, is the measure of deformation to a body's length due to a tensile or compressive axial load [8]. However, it does not describe the deformation caused by a fluid to a solid or the deformation of fluids in general, which is represented by volumetric strain [8]. The direct strain of a body is mathematically

defined as:

$$\epsilon = \frac{\Delta L}{L_0} = \frac{\delta}{L_0} \tag{1.4}$$

where L_0 is the body's original length in meters and depending on the preferred notation, δ or ΔL is the change in the body's length due to deformation in meters [8].

1.1.3.2 Volumetric Strain

Volumetric strain, or bulk strain, is the measure of deformation to a body's volume due to tensile or compressive load(s) on every side of the body [8]. The volumetric strain, or bulk strain, of a body is mathematically defined as:

$$Volumetric\ Strain = \frac{\Delta V}{V_0} \tag{1.5}$$

where ΔV is the change in the body's volume due to deformation in m^3 and V_0 is the body's original volume in m^3 [8]. Assuming the body is a cube, equation 1.5 can be simplified to:

$$\frac{\Delta V}{V_0} = \frac{L_0^3 - (L_0 - \delta)^3}{L_0^3} = 3 \cdot \frac{\delta}{L_0} = 3 \cdot \epsilon \tag{1.6}$$

where V_0 is the body's original volume in m^3, ΔV is the change in the body's volume in m^3, L_0 is the body's original length in m, and ϵ is the direct strain [8].

1.1.4 Bulk Modulus

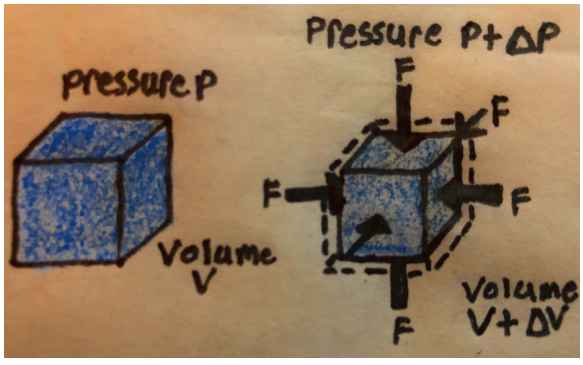

Figure 1.1: The figure illustrates a visual example of a substance's modulus of elasticity or bulk modulus.

The volumetric modulus of elasticity, or bulk modulus, is the measure of a body's resistance to compression due to an increased applied pressure on the body [8]. Bulk modulus can also be defined as the ratio of bulk stress to bulk strain or as the inverse of compressibility, β [8]. The bulk modulus of a body is mathematically defined as:

$$K = \frac{\Delta p}{\frac{\Delta V}{V_0}} = -V_0 \cdot \frac{dp}{dV} = \rho \cdot \frac{dp}{d\rho} \quad [Pa] \tag{1.7}$$

where K is volumetric modulus of elasticity in Pa, V_0 is the body's original volume in m^3, ΔV is the change in the body's volume in m^3, p is pressure in Pa, and ρ is the mass density of the body's material in kg/m^3 [8, 9]. Note, in some text, the volumetric modulus of elasticity is symbolized as E_v. Assuming the body is a cube, equation 1.7 can be simplified to:

$$K = \frac{volumetric\ stress}{volumetric\ strain} = \frac{\sigma}{3 \cdot \epsilon} \quad [Pa] \tag{1.8}$$

where σ is the stress in Pa and ϵ is the direct strain. The bulk modulus of an ideal gas undergoing an isotropic process, $\Delta Q_{therm} = 0$, is:

$$K_S = \rho \cdot \frac{dp}{d\rho} = \gamma \cdot p \quad [Pa] \tag{1.9}$$

where K_S is the isotropic bulk modulus in Pa, V is volume in m^3, ρ is mass density in kg/m^3, and γ is the ratio of specific heats [8, 9]. An ideal gas undergoing an isothermal process, $\Delta T = 0$ and $\Delta Q \neq 0$, has a bulk modulus given by:

$$K_T = -V_0 \cdot \frac{dp}{dV} = \rho \cdot \frac{dp}{d\rho} = p \quad [Pa] \tag{1.10}$$

where K_T is the isothermal bulk modulus in Pa, ρ is mass density in kg/m^3, γ is the ratio of specific heats, and p is pressure in Pa [8, 9].

1.1.5 Speed of Sound

The speed of sound is thermodynamic property, which defines the velocity an acoustic wave moves through a medium. In general, the speed of sound is defined as a

complex express, where the complex component represents absorption loss due to relaxation or other absorption mechanisms [2]. For a lossless acoustic wave, the speed of sound can be defined as:

$$c = \sqrt{\frac{\partial P(x,y,z)}{\partial \rho(x,y,z)}}_{isentropic} \quad \left[\frac{m}{s}\right] \tag{1.11}$$

where $P(x,y,z)$ is the instantaneous pressure in Pa and $\rho(x,y,z)$ is the mass density in kg/m^3 [2, 10]. In a perfect gas that is undergoing an isotropic process, equation 1.11 is extended using pressure and density relations define the speed of sound as:

$$c = \sqrt{\frac{\gamma \cdot P(x,y,z)}{\rho(x,y,z)}} = \sqrt{\gamma \cdot R \cdot T} = \sqrt{\frac{K}{\rho(x,y,z)}} \quad \left[\frac{m}{s}\right] \tag{1.12}$$

where $P(x,y,z)$ is the instantaneous pressure in Pa, γ is the specific heat ratio, R is the gas constant in $J/mol \cdot K$, T is the absolute temperature in kelvin, and K is the volumetric modulus of elasticity or bulk modulus in Pa [2, 10].

1.1.6 Pressure

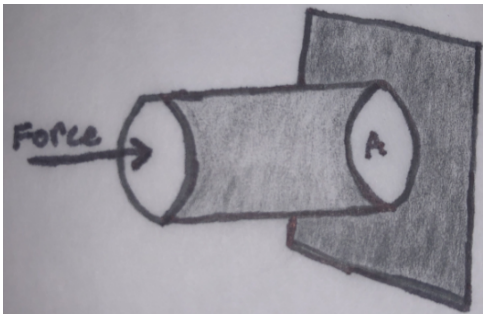

Figure 1.2: The figure shows an example of pressure with a normal force applied over a unit area.

Pressure is generally defined as:

$$p = \frac{F_n}{A} \quad [Pa] \tag{1.13}$$

where p is the pressure in Pa, F_n is the magnitude of the normal force vector applied over an area in newtons, and A is the surface area in m^2 [2]. An example of this

definition is seen in figure 1.2. The pressure at a point is defined as:

$$p = \frac{dF_n}{dA} \quad [Pa] \tag{1.14}$$

where dF_n is the magnitude of the infinitesimal force vector applied over an area in newtons and dA is the infinitesimal surface area in m^2. In either case, it can be shown mathematically that pressure is a measure of energy per unit volume, by multiplying the numerator and denominator of equation 1.13 by the distance moved. There are several different types of pressure, which are defined in the following sections.

1.1.6.1 Absolute, Gauge, & Atmospheric Pressure

The absolute pressure is measured relative to a perfect vacuum, which has an pressure of absolute zero [6]. The gauge pressure is measured relative to the local atmospheric pressure and can take values that are both positive or negative [6, 7]. When the gauge pressure is negative, it is commonly referred to as the vacuum pressure [6, 7]. The atmospheric pressure, also called the barometric pressure, is the force exert by a column of air on to the earth's surface, due to the effects of gravity [6, 10]. Therefore, the atmospheric pressure changes with elevation and slightly changes with weather conditions [10]. An approximation for atmospheric pressure in terms of the height above sea level is defined as:

$$p_{atm} = p_a \cdot \left(1 - \frac{B \cdot z}{T_0}\right)^{\left(\frac{g}{R \cdot B}\right)} \quad [Pa] \tag{1.15}$$

where p_a is the pressure at sea level in Pa, T_0 is the absolute temperature at sea level in kelvin, B is the lapse rate, z is the height above sea level in meters, g is the acceleration due to gravity, and R is the gas constant in $J/mol \cdot K$ [7]. The absolute pressure is defined as:

$$p_{absolute} = (p_{atm} + p_{gauge}) \quad [Pa] \tag{1.16}$$

where p_{atm} is the atmospheric pressure in Pa and p_{gauge} is the local pressure [7]. The equation can also be defined in terms of the ideal gas law [7].

1.1.6.2 Acoustic Pressure

The acoustic pressure is defined as:

$$p(x,y,z) = (P(x,y,z) - P_0(x,y,z)) \quad [Pa] \tag{1.17}$$

where p is the acoustic pressure in Pa, $P(x,y,z)$ is the instantaneous pressure Pa, and P_0 is the equilibrium pressure in Pa [2]. The equilibrium pressure, also known the ambient pressure, is default pressure in a system when there is no acoustic sound. The equation of state relates the thermodynamic properties of pressure, volume and temperature for a homogeneous material, where the equation varies with material and conditions [6]. The instantaneous pressure can be defined as the equation of state for a perfect gas given by:

$$P(x,y,z) = p(x,y,z) + P_0(x,y,z) = \rho(x,y,z) \cdot T_k \cdot r \quad [Pa] \tag{1.18}$$

where $\rho(x,y,z)$ is the mass density in kg/m^3, r is the specific gas constant and T_k is the absolute temperature in kelvin [2].

1.1.7 Particle Velocity

The particle velocity is the rate of change of the particle displacement and it is defined as:

$$u(x,t) = \frac{\partial \delta}{\partial t} \quad \left[\frac{m}{s}\right] \tag{1.19}$$

where δ is the particle displacement in meters and t is time in seconds. Using equation 1.19, the particle velocity for of a plane wave is derived as $u(x,t) = \frac{p(x,t)}{\rho_0 c}$ and thus, the pressure is $p(x,t) = u(x,t)\rho_0 c$ [2]. The root mean square particle velocity is defined as

$$u_{rms} = \frac{u}{\sqrt{2}} \quad \left[\frac{m}{s}\right] \tag{1.20}$$

where u is the particle velocity in m/s.

1.1.8 Volume Velocity

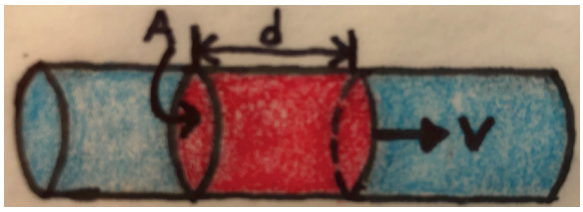

Figure 1.3: The figure shows an example of volume velocity.

The volume velocity (volume flow rate) is the velocity of a volume of fluid, which is detailed in figure 1.3 and given by:

$$U(x,t) = \frac{dV}{dt} = A \cdot \frac{d\delta}{dt} = A \cdot u(x,t) \quad \left[\frac{m^3}{s}\right] \tag{1.21}$$

where V is the volume of the fluid in m^3, A is the cross-sectional area of the volume in m^2, and $u(x,t)$ is the particle velocity in m/s. The root mean square of the volume velocity is given as:

$$U_{rms}(x,t) = \frac{U(x,t)}{\sqrt{2}} \quad \left[\frac{m^3}{s}\right] \tag{1.22}$$

where $U(x,t)$ is the volume velocity in m^3/s.

1.1.9 Impedance

Impedance is generally defined as the resistance caused by an restrictive element. In acoustics, impedance restricts the flow of an acoustic wave and it is defined with the following definitions.

1.1.9.1 Specific Acoustic Impedance

The impedance in terms of the particle velocity is called the specific acoustic impedance and it is given by:

$$z = \frac{p}{u} = r + ix \quad [\Omega] \tag{1.23}$$

where p is the acoustic pressure in Pa, u is the particle velocity in m/s, r is the real part of the impedance, and x is the complex part of the impedance [2].

1.1.9.2 Acoustic Impedance

The impedance in terms of the volume velocity is called the acoustic impedance and it is given by:

$$Z = \frac{p}{U} = \frac{p}{A \cdot \frac{d\delta}{dt}} = \frac{p}{A \cdot u} = \frac{z}{A} \quad [\Omega] \tag{1.24}$$

where A is the cross-sectional area of the volume in m^2, u is particle velocity in m/s, δ is particle displacement in meters, and U is the volume flow rate (volume velocity) in m^3/s [2].

1.1.10 Intensity

The intensity is the sound power per unit area or the rate at which work is done per unit area and it is defined as:

$$I(t) = p \cdot u \quad \left[\frac{W}{m^2}\right] \tag{1.25}$$

where p is the acoustic pressure in Pa and u is the particle velocity in m/s. The average acoustic intensity for a plane wave is given by:

$$I = < I(t) >_T = < pu >_T = \frac{1}{T}\int_0^T p \cdot u \cdot dt = \frac{P_A^2}{2 \cdot c \cdot \rho_0} = \frac{p_{rms}^2}{\rho_0 \cdot c} \tag{1.26}$$

where P_A is the amplitude of the acoustic amplitude in Pa, p_{rms} is the root mean square of the acoustic pressure in Pa, c is the speed of sound in m/s, and ρ_0 is the mass density in kg/m^3 [2, 5].

1.1.11 Sound Intensity Level & Sound Pressure Level

The acoustic pressures and intensities are generally reported in terms of logarithmic scales that are called sound levels [2]. This is common practice because of the large range of acoustic pressures and intensities [2]. The sound intensity level is defined as:

$$SIL = 10\, log_{10}\left(\frac{I}{I_{ref}}\right) \quad [dB] \tag{1.27}$$

where I is the intensity in W/m^2 and I_{ref} is the intensity reference in W/m^2. Using equation 1.26, the intensity level can be redefined as the sound pressure level, where the $\rho_0 c$ cancels out. The sound pressure level is the ratio of the root mean square pressure to a reference pressure and this is given by:

$$SPL = 20\,log_{10}\left(\frac{p}{p_0}\right) \quad [dB] \tag{1.28}$$

where p is the acoustic pressure and p_0 the reference pressure, which is usually 20 uPa [2].

1.1.12 Q-factor

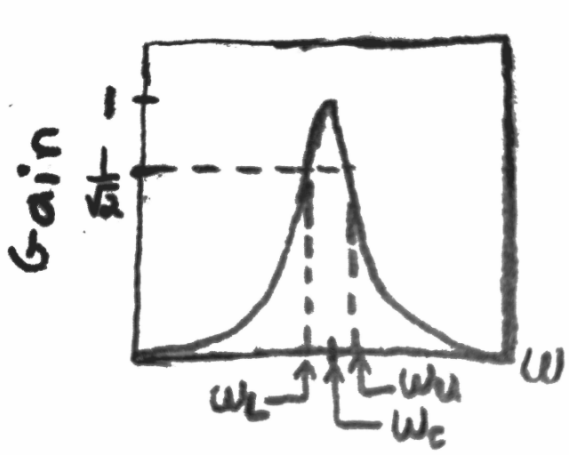

Figure 1.4: The quality factor of a resonance peak as shown in [2].

The quality factor can be defined in several ways, but the most common is a measurement of a resonance's sharpness, which is seen in figure [2]. The quality factor is defined as:

$$Q = \frac{f_U - f_L}{f_C} \tag{1.29}$$

where f_U is the upper negative 3db frequency in Hz, f_L is the lower negative 3db frequency in Hz, and f_C is the center frequency in Hz. However, a more general

definition of the quality factor is given by:

$$Q = \frac{\omega \cdot E_{stored}}{P_{radiated}} \tag{1.30}$$

where ω is the angular frequency in rad/s, E_{stored} is the energy stored in J and $P_{radiated}$ is the power radiated in W. The more general definition can be written in an alternate form that uses the equivalent electrical circuit of an acoustical system.

1.1.13 Capacitor

A capacitor is an electrical component that stores energy in an electric field. The most basic design of a capacitor uses two parallel plates that are separated by a dielectric (material that is not conductive), which creates an electric field between the two plates. The dielectric restricts current flow between the two plates which results in the plates accumulating charge. Negative charge accumulates on one plate and coulomb's force exerts a repealing force on any negative charge still on the other plate, which results in the other plate being positively charged. The electric field results from each charge creating a small electric field due to coulomb law. Therefore, capacitors do not store energy by storing charge as seen in batteries, but by creating an electric field that creates a potential difference between the plates. The amount of charged stored on one plate is represented by:

$$Q(t) = C \cdot V(t) \quad [A \cdot s] \tag{1.31}$$

where $Q(t)$ is the charge at time t in coulombs and $V(t)$ is the voltage at time t in volts. The previous equation 1.31 can be expanded by defining the rate of change in charge on a plate as the current across the capacitor, which is given by:

$$dQ(t) = C \cdot dV(t) \quad [A \cdot s] \tag{1.32}$$

The current across the capacitor is given by:

$$I(t) = \frac{dQ(t)}{dt} = C \cdot \frac{dV(t)}{dt} \quad [A] \tag{1.33}$$

A real-world capacitor has parasitic resistance and inductance. The parasitic resistance is due to equivalent series resistance and leakage.

1.1.14 Inductor

An inductor is an electrical component, which consist of a coil of wire that is normally wrapped around some type of core, that stores energy in a magnetic field. The inductor acts as an inertial force on the change in current through the inductor. The voltage across the inductor is defined as:

$$V(t) = L \cdot \frac{di(t)}{dt} \quad [V] \tag{1.34}$$

The current across the inductor is found by using equation 1.34 and solve for current, which is given as:

$$i(t) = \frac{1}{L}\left(\int_0^T v(t) \cdot dt\right) + i_0 \quad [A] \tag{1.35}$$

1.1.15 Resonators

There are several types of acoustic resonators, such as, the quarter wavelength resonator, a Helmholtz resonator, or a open tube resonator. However, Helmholtz resonators were almost exclusively used in the creation of the acoustic metamaterials in this project.

1.1.15.1 Critical Coupling

The term critical coupling is another term for maximum power transfer between a resonator and the coupled element.

1.1.15.2 Helmholtz Resonator

Figure 1.5: The figure shows various types of Helmholtz resonators as shown in [2].

A Helmholtz resonator (HR) is a container of fluid, usually air, that has a hole in the form of a neck or port, as seen in figure 1.5. For the purposes of this paper, a HR is defined as having a neck, as seen in (a) in figure 1.5. A HR creates an acoustic wave at the resonance frequency when fluid, usually air, flows into the neck. The fluid flowing into the neck, the driving force, creates an oscillating acoustic wave when it is oscillating at or near the resonance frequency. The HR can be roughly modeled with a linear mass spring system with the air in the neck acting as a mass and the fluid flow comprising the fluid in the cavity, creating a spring like compression. In addition, the HR can be modeled using an RLC circuit, where the inductor represents the inertia of the mass not to move, the resistance represents the lossy nature of the physical system, and the capacitor represents the stored potential energy when a pressure wave compresses air in the cavity of the resonator. The equivalent RLC circuit for modeling a HR, seen in figure 1.6, is only valid when the lumped element approximation is valid to use.

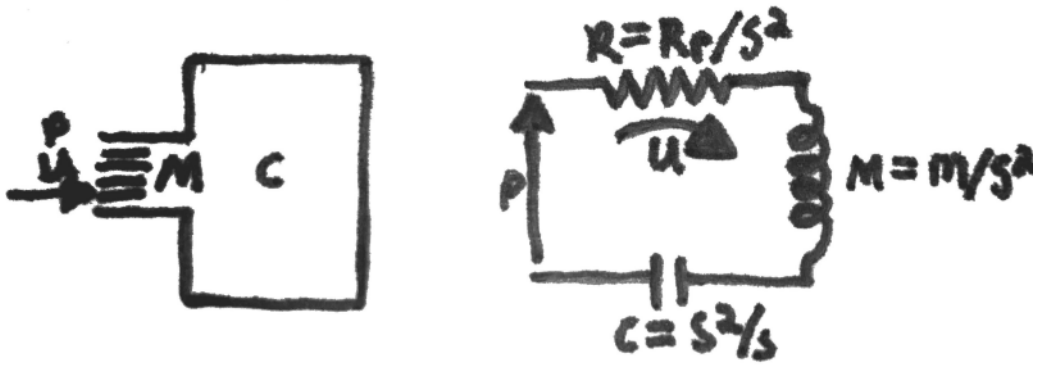

Figure 1.6: The figure shows the equivalent RLC circuit of a HR as shown in [2].

The resonance frequency of a HR is given in text as:

$$f_{HR} = \frac{c}{2\pi} \cdot \sqrt{\frac{S}{V(l+\delta l)}} \quad [Hz] \tag{1.36}$$

where c is the speed of sound in m/s, S is the cross sectional area of the neck in m^2, V is the volume of the cavity in m^3, l is the length of the neck in meters, and δl is the neck length adjustment in meters [2].

The direct derivation of equation 1.36 is not possible because it is a 2nd order Taylor approximation of a transcendental equation, which is found with the force equations [11]. The resonance frequency is generally dependent on the shape of the HR, because of it's affect on the force equations. However, this is a very weak dependence for the first harmonic of the resonance frequency and it is generally considered independent of shape [2, 5].

Assuming the dimensions of the HR are smaller than the operating wavelength, the equation can also be derived using an equivalent electrical system, using the lumped element method [2, 5]. The reactance of the HR is given by:

$$X = L \cdot \omega - \frac{1}{\omega \cdot C} \quad [\Omega] \tag{1.37}$$

where L is the inductance equal to $\frac{m}{A^2}$ in H, m is the mass of air in the neck in kg, A is the cross sectional area of the neck in m^2, C is the capacitance equal to $\frac{A^2}{S}$ in F,

S is the stiffness, and ω is the angular frequency in rad/s [5].

A HR attached to a waveguide is called a side branch HR, which can also be represented using an equivalent electrical circuit. A side branch HR is represented by the impedance of the HR in parallel with the impedance of the waveguide [2, 5]. The transmission coefficient of a waveguide with a branch is given by:

$$T_{Coeff}\left(\omega\right) = \frac{W_t(\omega)}{W_i(\omega)} = \frac{R_g^2 + X_g(\omega)^2}{(\frac{c\cdot\rho_0}{2\cdot A} + R_g)^2 + X_g(\omega)^2} \tag{1.38}$$

where W_t is the sound power transmitted in watts, W_i is the sound power incident in watts, A is the cross-sectional area of the waveguide in m^2, ρ_0 is the mass density of the fluid in kg/m^3, X_g is the reactance of the branch in ohms, R_g is the resistance of the branch in ohms, and ω is the angular frequency in rad/s [5]. Equation 1.38, can be simplified to the transmission coefficient of a waveguide with a side branch HR by substituting equation 1.37 for X_g and assuming R_g is approximately zero for the ideal case [5]. Therefore, the transmission coefficient of the waveguide with a HR as a side branch for the ideal case is given as:

$$T_{Coeff}\left(\omega\right) = \frac{x_g(\omega)^2}{x_g(\omega)^2 + (\frac{\rho_0\cdot c}{2\cdot A})^2} = \left[1 + \frac{c^2}{4\cdot A^2(\frac{\omega\cdot L^{'}}{A_g} - \frac{c^2}{\omega\cdot V})}\right]^{-1} \tag{1.39}$$

where A is the cross-sectional area of the waveguide in m^2, A_g is the cross-sectional area of the neck of the HR in m^2, $L^{'}$ is the corrected length of the HR's neck in meters, V is the cavity volume of the HR in m^3, c is the speed of sound in m/s, and ω is angular frequency in rad/s [5]. The resonance frequency of a waveguide with a side branch HR is derived by setting equation 1.39 equal to zero and solving for ω, which gives equation 1.36 [5].

A waveguide with N number of parallel side branch HRs has a transmission coefficient of:

$$T_{Coeff}\left(\omega\right) = \frac{2\cdot Z_{HR}\left(\omega\right)}{N\cdot Z + 2\cdot Z_{HR}\left(\omega\right)} = \frac{2\cdot Z_{HR}\left(\omega\right)}{N\cdot\frac{\rho\cdot c}{S_{wave}} + 2\cdot Z_{HR}\left(\omega\right)} \tag{1.40}$$

where ω is the angular frequency in rad/s, Z_{HR} is the impedance in ohms of a HR in terms of the angular frequency, N is the number of HRs in parallel with each other, Z is the impedance in ohms of the waveguide, S_{wave} is the surface area of the waveguide in m, ρ is the mass density in kg/m^3, and c is the speed of sound in m/s. Using equation 1.39 and 1.40, a waveguide with two parallel HRs side branch to a waveguide with an ideal resistance of zero has a transmission coefficient given by:

$$T_{Coeff}(\omega) = \frac{x_g(\omega)^2}{x_g(\omega)^2 + (\frac{\rho_0 * c}{2 * A})^2} = [1 + \frac{c^2}{A^2(\frac{\omega L'}{A_g} - \frac{c^2}{\omega V})}]^{-1} \tag{1.41}$$

Using the equation, the resonance frequency is determined to be the same as the waveguide with the single branch HR. However, the realistic resonance frequency is slightly shifted from the individual resonance [12].

1.1.16 Continuity Equation

The conservation of mass principle is applied to the steady fluid flow through a duct, which gives the continuity equation as:

$$\rho_1 \cdot A_1 \cdot V_1 = \rho_2 \cdot A_2 \cdot V_2 \tag{1.42}$$

where A is the cross-sectional area of the structure at the point of interest in m^2, V is the velocity in m/s, and ρ is the mass density in kg/m^3 [6].

1.1.17 Bernoulli's Equation

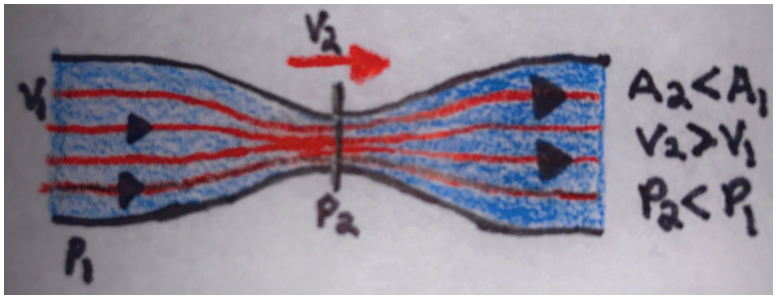

Figure 1.7: The figure shows an example of when Bernoulli's equation would be used.

The Navier-Stokes can be simplified into the linearized Euler's equation, which can be simplified into Bernoulli's equation, by assuming the flow is steady, inviscid, and it is along a streamline. Bernoulli's equation is used to describe the fluid flow through a structure as seen in figure and it is given by:

$$P_1 + \frac{1}{2} \cdot \rho \cdot v_1^2 + \rho \cdot g \cdot h_1 = P_2 + \frac{1}{2} \cdot \rho \cdot v_2^2 + \rho \cdot g \cdot h_2 \tag{1.43}$$

where P_1 is the pressure at the inlet in Pa, P_2 is the pressure at the point of interest in Pa, ρ is the mass density in kg/m^3, V_1 is the particle velocity at the inlet in m/s, h_1 is the height of the inlet in meters, and g is the acceleration due to gravity in m/s^2.

1.1.18 Brake Horsepower

Horsepower (hp) is the rate of work done over a period of time, which is a unit of power [13]. There are many different types of horsepower, such as, mechanical horsepower or electrical horsepower [13]. Horsepower can be defined mechanically in terms of angular velocity and torque, given by:

$$P_{hp} = \tau \cdot \omega \quad \left[N \cdot m \cdot \frac{rad}{s}\right] = \frac{T \cdot N}{5252} \quad \left[\frac{ft \cdot lbf \cdot rev}{min}\right] \tag{1.44}$$

where τ is torque in $N \cdot m$, ω is angular velocity in rad/s, T is torque in $ft \cdot lbf$, and N is the rotational speed in rev/min [13]. The unit of hp can be converted to watts, the unit of electrical power, where the conversion is defined by:

$$1\ [hp] = 745.7 \quad [W] \tag{1.45}$$

The brake horsepower (bhp) is the power provided to the shaft by the motor, when a brake is applied to the shaft, which is determined by the motor's efficiency or by:

$$P_{bhp} = \frac{\frac{\gamma \cdot Q \cdot h}{33000}}{\eta_{fan}} \quad [hp] \tag{1.46}$$

where γ is the specific weight, Q is the volumetric airflow rate in ft^3/min, h is the head in ft, and η_{fan} is the fan's efficiency [13]. The efficiency of the motor to convert

electrical power to shaft power is given by:

$$\eta_{motor} = \frac{P_{bhp}}{P_{hp_elec}} \tag{1.47}$$

where η_{motor} is the efficiency of the motor, P_{bhp} is the brake horsepower, and P_{hp_elec} is the electric power in hp [13]. The brake horsepower can be defined in terms of voltage by combining the previous equations, which is given by:

$$P_{bhp}(V) = \frac{\frac{(V \cdot I)}{746}}{\eta_{motor}} \quad [hp] \tag{1.48}$$

where η_{motor} is the fan motor's efficiency, V is the input voltage to the motor, and I is the input current that is constant for this equation [14].

1.1.19 Fan Affinity Laws

The fan affinity laws were derived using the dimensional analysis' pi theorem and it is assumed that the fan's efficiency stays the same [15]. However, the fan's efficiency never stays the same with changes to various conditions, but it allows for close approximations in most cases [15]. The more accurate approach is use the fan's known data from a fan curve and interpolate the required values, but this approach is not always possible [15]. The affinity laws are defined as:

$$\frac{Q_1}{Q_2} = \left(\frac{d_1}{d_2}\right)^3 \cdot \frac{N_1}{N_2} \tag{1.49}$$

$$\frac{P_{bhp-1}}{P_{bhp-2}} = \left(\frac{N_1}{N_2}\right)^2 \cdot \left(\frac{d_1}{d_2}\right)^2 \tag{1.50}$$

$$\frac{SP_1}{SP_2} = \left(\frac{n_1}{n_2}\right)^3 \cdot \left(\frac{d_1}{d_2}\right)^5 \tag{1.51}$$

where d_1 is the first fans' diameter in ft, P_{bhp-1} is the first fans' brake horsepower in hp, N_1 is the first fans' rotational velocity in rev/min, Q_1 is the first fans' volumetric airflow rate in ft^3/min, and SP_1 is the first fans' static pressure in inches of water

column [14].

1.1.19.1 Airflow Velocity

The average airflow velocity at a given point inside a flow channel or duct can be calculated by dividing the volumetric airflow rate at that point by the cross-sectional area of the flow channel at that point, which is given by:

$$V_{air} = \frac{Q}{S_{Fan}} \quad \left[\frac{ft}{min}\right] \tag{1.52}$$

where Q is the volumetric airflow rate in ft^3/min and S_{Fan} is the cross-sectional area of the fan channel in ft^2.

1.1.20 Fan Noise

Fan noise is noise caused by noise sources, such as, the fan blades or the internal parts of a motor. The sources of fan noises may be dependent on factors, such as, the fan's type, the fan motor type, and the fan motor placement [16, 17, 18, 19]. The main sources of fan noise for the Sofasco fan are the sleeve bearing rotation frequency (SBRF) and the blade pass frequency (BPF), which is seen in the Fan characteristics section of this chapter.

1.1.20.1 Sleeve Bearing Rotation Frequency

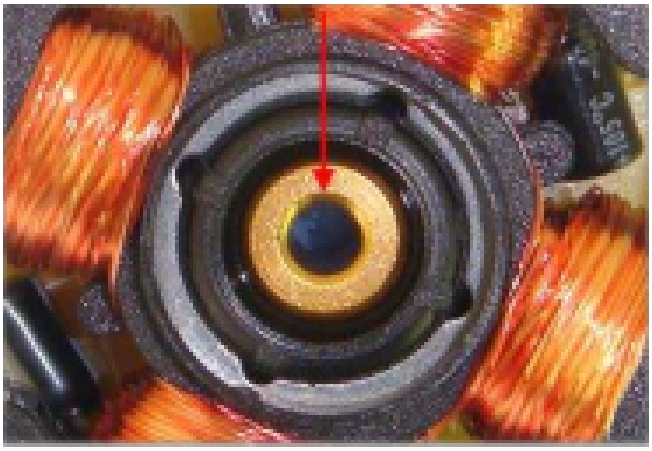

Figure 1.8: The figure displays the internals parts of a computer fan motor and the red arrow identifies the fan's sleeve bearing.

The Fan Rotation Frequency (FRF), which is also known as the Sleeve Bearing Rotation Frequency, is the resonance frequency of the fan due to the fan rotation causing a friction force on the bearing [18, 19]. Figure 1.8 shows the internal parts of a computer fan motor and the red arrow identifies the fan's sleeve bearing. The SBRF and its' overtones can be calculated using the following equation

$$SBRF_n = n \cdot \frac{RPM}{60} \quad [Hz] \tag{1.53}$$

where n is harmonic number and RPM is the revolutions per minute.

1.1.20.2 Blade Pass Frequency

The Blade Pass Frequency (BPF) is the resonance frequency of the fan due to each blade passing a set point and pushing air forwards causing a pressure wave [17]. The BPF and its' overtones can be calculated with the following equation:

$$BPF_n = n \cdot \frac{(RPM) \cdot (Number\ of\ Blades)}{60} \quad [Hz] \tag{1.54}$$

where n is the harmonic number and RPM is revolutions per minute. This equation can be expanded to be in terms of the fan motor's voltage, which is given by:

$$BPF_n(V) = n \cdot \left[\frac{(Number\ of\ Blades) \cdot RPM(V)}{60} \right] \quad [Hz] \tag{1.55}$$

where $RPM(V)$ is the revolutions per minute in terms of voltage and n is the harmonic number.

1.1.20.3 Number of Blades

The number of blades the fan has can be calculated with a ratio of the BPF and the SBRF. The ratio that gives the number of blades is given by:

$$Number\ of\ Blades = \frac{BPF}{SBRF} \tag{1.56}$$

1.1.21 Metamaterials

There is not an exact definition for a metamaterial, because it would be different for each field that uses metamaterials. A general definition is a material made of a lattice of unit cells that are significantly smaller the the wavelength of interest. The properties of a metamaterial, typically, do not naturally occur in nature, such as, an optical or acoustic metamaterial with a negative refractive index. These properties are from the structure and not the individual components that make up the material.

1.1.21.1 Acoustic Metamaterials

The propagation of acoustic waves cane be described with the linearized acoustic wave equation, which is given by:

$$\nabla^2 P - \frac{1}{c^2}\frac{\partial^2 P}{\partial t^2} = 0 \tag{1.57}$$

where P is the acoustic pressure in Pa and c is the speed of sound in m/s [2]. Assuming the material the acoustic wave is traveling through is perfect gas and an adiabatic as discussed in the speed of sound section, then the speed of sound can be given by equation 1.12. The linearized acoustic wave equation can be rewritten from equation 1.12 to give:

$$\nabla^2 P - \frac{\rho}{K}\frac{\partial^2 P}{\partial t^2} = 0 \tag{1.58}$$

where ρ is the mass density in kg/m^3, K is the bulk modulus in Pa, and P is the acoustic pressure in Pa [3]. The acoustic refractive index is given by:

$$n = \sqrt{\frac{\rho_r}{K_r}} \tag{1.59}$$

where ρ_r is the relative mass density given as ρ/ρ_0 and K_r is the relative bulk modulus given as K/K_0 [3]. The mass density of air, ρ_0, is approximately 1.22 kg/m^3 and the bulk modulus of air, K_0, is approximately $1.42 \cdot 10^5$ Pa. The acoustic refractive index can be equal to the inverse of the relative speed of sound under certain conditions,

but this is not always the case. The acoustic impedance can be defined using mass density and the bulk modulus by:

$$Z = \sqrt{\rho \cdot K} \quad [\Omega] \tag{1.60}$$

where ρ is the mass density in kg/m^3 and K is the bulk modulus in Pa [3]. These equations can be used to characterize the acoustic wave and its' propagation through space. In conventional media, the mass density and bulk modulus are always positive values in nature, but their effective values can be negative in a metamaterial [3]. Acoustic metamaterials can be classified using the sign of the mass density and bulk density or the sign of the refractive index [3]. The graph in figure 1.9 classifies acoustic metamaterials in four quadrants, where a metamaterial with all positive values like a conventional material is found in the right upper quadrant.

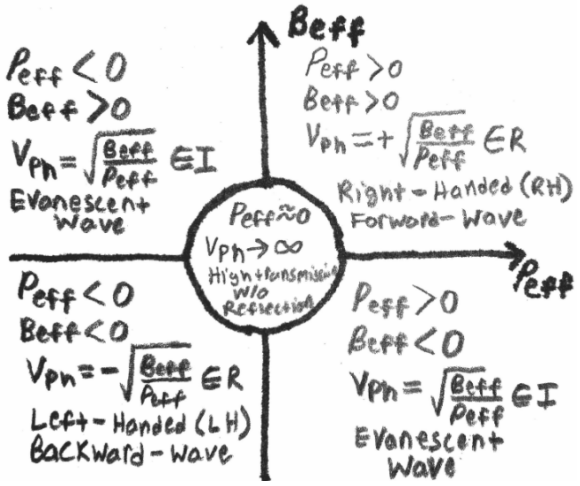

Figure 1.9: The figure shows a graph with the classification of acoustic metamaterials by the value of mass density and bulk modulus. The graph was taken from [3].

1.2 Literature Review

The following papers, listed as subsections in this section, have concepts and/or theory that was helpful in the design of the acoustic metamaterial. The subsections contain a summary of each of the papers.

1.2.1 Silencer design by using array resonators for low-frequency band noise reduction

In this article, Sang-Hyun and Yang-Hann investigate the effect of HRs (Helmholtz Resonators) along a waveguide and how their arrangement effects noise attenuation. In addition, they studied the acoustic properties of arrays of HRs and an equivalent impedance for the whole silencer. The equivalent impedance was used to determine the resonance frequencies and create an optimization algorithm for HR placement. Their goal was to determine a way using array of HRs to broaden the narrow noise attenuation of a single HR. They start by using the transfer matrix method and lumped element approximation to determine the impedance of a single HR as a side branch and the impedance of the waveguide, which is used to estimate the transmission loss. Their results for the single resonator setup are easily found in most acoustic textbooks [5]. They continued by conducting experiments with arrays of HRs arranged in series and then in parallel along a waveguide. The transmission coefficient for N unit cells with identical HRS in parallel is defined as:

$$T_{coeff} = \frac{2 * Z_H R}{N * Z + 2 * Z_{HR}} \tag{1.61}$$

where $Z_H R$ is impedance of one HR, N is the number of unit cells, Z is the characteristic impedance defined as $c * /rho/A$, A is the cross-sectional area of the waveguide. Their results showed that HRs arranged in series would mainly increase the magnitude of the transmission loss at resonance, but HRs arranged in parallel were shown to logarithmically increase the transmission loss and bandwidth near resonance. They concluded multiple frequencies can be targeted using multiple arrays of HRs at different resonances. They explored how changing the spacing between the HRs changed the transmission loss and they found that the maximum transmission loss occurs when they are space $\lambda/4$ apart. The spacing of the HRs had a large impact on the transmission loss than the arrangement of the HRs, but they noted there is a draw

back when targeting low frequency sound, as the waveguide would need to be large and long. They determine that the maximum transmission loss occurs when the HRs are spaced at distance of:

$$L_i = \frac{\frac{1}{\lambda_i} + \frac{1}{\lambda_{i+1}}}{2} = \frac{c(\frac{1}{f_i} + \frac{1}{f_{i+1}})}{8} \tag{1.62}$$

where i is the index to represent the different HRs [20]. They end the paper by presenting an optimization method for determining the distance between the HRs based on the desired transmission loss and the bandwidth of the transmission loss.

1.2.2 Redesigning Helmholtz resonators to achieve attenuation at multiple frequencies

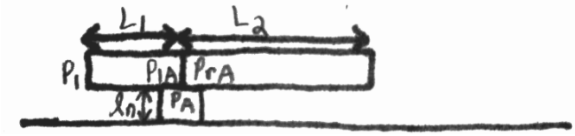

Figure 1.10: The figure as shown in the paper, shows how the author defined different volumes in the HR's cavity.

In this paper, Etaix and Nicolas investigate how to target multiple frequencies for sound attenuation using HRs (Helmholtz Resonators). Sound attenuation targeting multiple frequencies using HRs is normally achieved arranging multiple HRs in either series or parallel, but in this article they introduce a new strategy. They introduce a method to achieve attenuation at multiple frequencies using a single HR using higher order modes in the HR's cavity. They achieve this by changing the location of the HR's neck relative to its' cavity. The impedance of a HR that is commonly found in an acoustic textbook can not be used to model this method because it treats the cavity as one volume. They begin deriving a new impression for the HR's impedance by defining two volumes in the cavity, where the neck's location relative to the cavity is the separation between the two volumes, which can be seen in figure. They continued by using the transfer matrix method and defined the impedance as

well as the transfer loss. They showed that this method could be expanded to target multiple frequencies with a single HR by using multiple HRs. The effect of the cavity's shape on the resonance frequency at each mode was investigated and they found that at the first resonance frequency was approximately independent of the shape, but the higher order frequencies were dependent on the shape of the cavity. They concluded that the design process for creating multiple frequencies from a single HR is to first choose the first frequency by choosing a volume and then tune the second frequency by adjusting the dimensions of the cavity.

1.2.3 Benchmark Analysis of a Helmholtz Resonator for Estimating Acoustic Metamaterial Properties

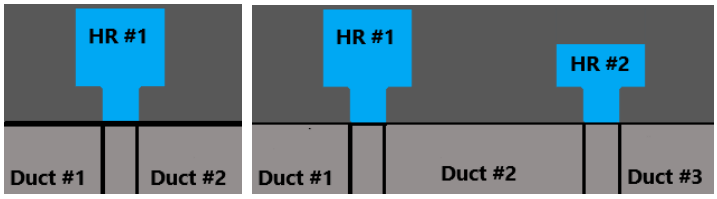

Figure 1.11: The figure shows the metamaterial unit cells explored in the article. The first image shows a unit cell with a single HR and the second image shows a unit cell made of two series HRs. The unit cells were connected to the impedance tube where the sample holder is normally placed.

In this article, Mohapatra and Jena describe a method for estimating acoustic metamaterial properties such as effective mass density and effective bulk modulus [21]. In both scenarios, the waveguide is part of the unit cell as seen in figure 1.11. Metamaterials are defined by the authors as materials with properties that do not naturally occur in nature [21]. A classification for metamaterials that is commonly used in the field is introduced, which states that metamaterials can be classified by their refractive index, being zero or negative. However, this classification neglects a region that is defined in other metamaterial classifications [3]. The acoustic refractive index is described as being controlled by the effective mass density or effective bulk modulus or both. The unit cells shown in figure 1.11 are analytically modeled by

first calculating the impedance of each HR used in either unit cell [21].The authors calculate an estimate for each HR impedance using the electro-acoustic modeling theory, which uses an electrical model to estimate acoustic properties, but this is not the only method that could have been used to calculate each impedance [21]. The impedance of a HR is generally defined by:

$$Z_{HR}(\omega) = \frac{\omega^2}{\pi c^2} + j[\omega \frac{l_{eq}}{S_n} - \frac{c^2}{\omega V_c}] \tag{1.63}$$

where ω is the angular frequency, c is the speed of sound in m/s, l_{eq} is the equivalent neck length in meters, S_n is the cross-sectional area of the neck in m^2, and V_c is the volume of the cavity in m^3 [21]. The equivalent neck length contains the neck correction and it is defined in the article as:

$$l_{eq} = l_n + 1.7 r_n \tag{1.64}$$

where l_n is the neck length in meters and r_n is the neck radius in meters [21]. The analytical modeling of the unit cells continues by using the acoustic transfer matrix theory and the impedance of each HR to calculate the TM of each HR. The TM of each HR is calculated using a general equation derived by the transfer matrix theory for a single HR, which is given by:

$$TM_{HR}(\omega) = \begin{bmatrix} 1 & 0 \\ Z_{HR}^{-1}(\omega) & 1 \end{bmatrix} = \begin{bmatrix} 1 & 0 \\ \frac{1}{Z_{HR}(\omega)} & 1 \end{bmatrix} \tag{1.65}$$

where $TM_{HR}(\omega)$ is the transfer matrix for a single HR at a specific angular frequency, $Z_{HR}(\omega)$ is the estimated impedance of a single HR in terms of angular frequency [21]. The TM for each section of waveguide, or duct using the authors' terminology, is calculated using a commonly known definition from the transfer matrix theory of linear acoustics, but an expression for the duct's TM could have been derived using a calculated impedance, similar to the method used for the HR [21]. The TM for the duct is generally defined as:

$$TM_{duct} = \begin{bmatrix} cos(kl_r) & -jY_r sin(kl_r) \\ \frac{-j}{Y_r} sin(kl_r) & cos(kl_r) \end{bmatrix} = \begin{bmatrix} cos(kl_r) & -jY_r sin(kl_r) \\ \frac{-j\pi d_r^2}{c} sin(kl_r) & cos(kl_r) \end{bmatrix} \tag{1.66}$$

where Y_r is a constant, l_r is the duct length in meters, d_r is the duct radius in meters, and c is the speed of sound in $\frac{m}{s}$ [21]. The analytical model for the unit cells are defined as TMs and they are given by:

$$TM^1(\omega) = TM_{duct-1} \cdot TM_{HR-1}(\omega) \cdot TM_{duct-2} \tag{1.67}$$

$$TM^2(\omega) = TM_{duct-1} \cdot TM_{HR-1}(\omega) \cdot TM_{duct-2} \cdot TM_{HR-2}(\omega) \cdot TM_{duct-3} \tag{1.68}$$

where $TM^1(\omega)$ is the TM of the unit cell with a single HR in terms of angular frequency as shown in the first image of figure 1.11, $TM^2(\omega)$ is the TM of the unit cell with two HRs in terms of angular frequency as shown in the second image of figure 1.11, TM_{duct-1} is the first section of duct in the unit cell and $TM_{HR-1}(\omega)$ is the TM of the first HR in the unit cell in terms of angular frequency [21]. Each unit cell transfer matrix has a general form given as:

$$TM^1(\omega) = \begin{Bmatrix} TM_{11}^1(\omega) & TM_{12}^1(\omega) \\ TM_{21}^1(\omega) & TM_{22}^1(\omega) \end{Bmatrix} \tag{1.69}$$

$$TM^1(\omega) = \begin{Bmatrix} TM_{11}^1(\omega) & TM_{12}^1(\omega) \\ TM_{21}^1(\omega) & TM_{22}^1(\omega) \end{Bmatrix} \tag{1.70}$$

$$TM^2(\omega) = \begin{Bmatrix} TM_{11}^2(\omega) & TM_{12}^2(\omega) \\ TM_{21}^2(\omega) & TM_{22}^2(\omega) \end{Bmatrix} \tag{1.71}$$

The authors describe how the transmission coefficient and the reflection coefficient of either acoustic metamaterial can be extracted using the corresponding transfer matrix. Using the elements of the transfer matrix for the desired setup, the reflection

and transmission coefficients are defined as:

$$R(\omega) = \frac{T_{11}(\omega) - \rho \cdot c \cdot T_{21}(\omega)}{T_{11}(\omega) + \rho \cdot c \cdot T_{21}(\omega)} \tag{1.72}$$

$$T(\omega) = \frac{2e^{j \cdot k(\omega) \cdot d}}{T_{11}(\omega) + (T_{12}(\omega)/\rho \cdot c) + \rho \cdot c \cdot T_{21}(\omega) + T_{22}(\omega)} \tag{1.73}$$

where k is the wave number in rad/m, ρ is mass density in kg/m^3, c is the speed of sound in $\frac{m}{s}$, and d is the length or thickness of the sample in meters [21, 22]. The effective acoustic impedance and the effective refractive index can be defined using the transmission coefficient and the reflection coefficient as:

$$Z_{eff}(\omega) = \frac{r(\omega)}{1 - 2 \cdot R_{coeff}(\omega) - R_{coeff}(\omega)^2 - T_{coeff}(\omega)^2} \tag{1.74}$$

$$n_{eff}(\omega) = \frac{-j \cdot log_{10}(x(\omega)) + 2 \cdot \pi \cdot m}{k(\omega) \cdot d} \tag{1.75}$$

where $R_{coeff}(\omega)$ is the reflection coefficient in terms of angular frequency, $T_{coeff}(\omega)$ is the transmission coefficient in terms of angular frequency, $k(\omega)$ is the wave number in terms of the angular frequency in rad/m, d is the thickness or length of the meta-material in meters, and m is the branch number for the logarithm, a multi-variable function, which can estimated using the Kramers-Kronig relation [21, 22, 23]. In the previous equations, $r(\omega)$ and $x(\omega)$ are defined as:

$$r(\omega) = \sqrt{(R_{coeff}(\omega)^2 - T_{coeff}(\omega)^2 - 1)^2 - 4 \cdot T_{coeff}(\omega)^2} \tag{1.76}$$

$$x(\omega) = \frac{1 - R_{coeff}(\omega)^2 + T_{coeff}(\omega)^2 + r}{2 \cdot T_{coeff}(\omega)} \tag{1.77}$$

where $T_{Coeff}(\omega)$ is the transmission coefficient in terms of angular frequency and $R_{Coeff}(\omega)$ is the transmission coefficient in terms of angular frequency. Finally, the authors show that the effective bulk modulus and the effective mass density are defined as:

$$K_{eff}(\omega) = K_0 \cdot \frac{n_{eff}(\omega)}{Z_{eff}(\omega)} \quad [Pa] \tag{1.78}$$

$$\rho_{eff}(\omega) = \rho_0 \cdot n_{eff}(\omega) \cdot Z_{eff}(\omega) \quad \left[\frac{kg}{m^3}\right] \tag{1.79}$$

where ω is the angular frequency in rad/s, $K_{eff}(\omega)$ is the effective bulk modulus in Pa, $\rho_{eff}(\omega)$ is effective mass density in kg/m^3, $Z_{eff}(\omega)$ is the effective impedance in ohms, ρ_0 is the mass density in air, and K_0 is the bulk modulus in air. The mass density in air at STP (Standard Pressure and Temperature) is 1.22 kg/m^3 and the bulk modulus in air at STP is $1.42 \cdot 10^5$ Pa [24]. The authors state the transmission loss can be estimated using the transmission coefficient as:

$$TL(\omega) = 10 \cdot log_{10}\left(\frac{1}{T_{Coeff}(\omega)}\right) = 10 \cdot log_{10}\left(\frac{W_i(\omega)}{W_t(\omega)}\right) \quad [dB] \tag{1.80}$$

where $T_{Coeff}(\omega)$ is the transmission coefficient in terms of angular frequency, W_i is the incident power in watts and W_t is the transmitted power in watts.

1.3 Fan Characteristics

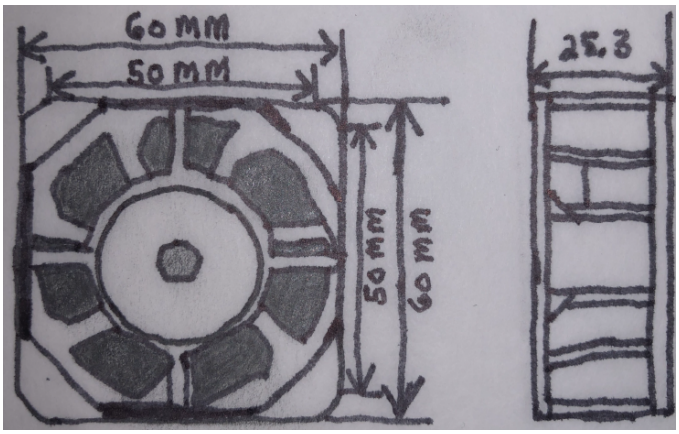

Figure 1.12: The figure is a drawing of the CAD model for a Sofasco D6025V12SHBL-03 fan with the fan's dimensions, which was provided by the manufacturer online.

The data sheet for the Sofasco D6025-03 series fans is provided on the manufacturer's website [1]. The data sheet provides specifications for various Sofasco D6025-03 series fans, including the Sofasco D6025V12SHBL-03 cooling fan, which is the one chosen by the Harris corporation for noise attenuation. A CAD model of the Sofasco

D6025V12SHBL-03 cooling fan with labeled dimensions is shown in figure 1.12 and the manufacturer provided it on their website. The Sofasco fan has axial flow and thus, it is classified as a axial flow fan, which has a direct drive dc motor [7, 6]. According to figure 1.12, the fan's airflow channel has a diameter of approximately 60 mm and thus, a radius of approximately 30 mm. The cross-sectional area of the fan's airflow channel is equal to:

$$S_{Fan-Channel} = \pi \cdot r^2 = 90 \cdot \pi \ [mm^2] = 0.0304 \ [ft^2] \tag{1.81}$$

The important properties of the the Sofasco D6025V12SHBL-03 cooling fan that are found on the fan's data sheet are listed in table 1.1. The airflow rate, also known as the volumetric velocity, is the volume of air that pass through a fixed unit area over a set amount of time [6]. The airflow rate of the Sofasco fan, which is given in table 1.1 can be used to calculate the air velocity [6]. Using equation 1.52, the air velocity for the fan operating at the rated 12 volts is equal to 1261 ft/min.

Table 1.1: The table list properties of the Sofasco cooling fan [1].

Rated Operating Voltage [V]	Operating Voltages [V]	Rated Operating Current [A]	Input Power [W]	Rotational Speed [RPM]	Max Pressure [Pa]	Airflow Rate [m^3/ min]
12	10.2 - 13.8	0.39	4.68	7000	131.41	1.09

The fan generates two main types of noise, which occur at harmonics of the BPF (Blade pass frequency) and the SBRF (Sleeve bearing rotation frequency) [17]. The BPF and SBRF are calculated with equations 1.54 and 1.53, which are used to calculate the first five harmonics that are found in table 1.2 for a fan operating at the rated operating voltage [17].

Table 1.2: The table lists the first 5 harmonics of the fan's BPF and SBRF.

Harmonic #	Calculated BPF [Hz]	Calculated SBRF [Hz]	Number of Blades
1	817	117	6.98
2	1634	234	6.98
3	2451	351	6.98
4	3268	468	6.98
5	4085	585	6.98

In table 1.2, the last column lists the number of blades used by the fan and this is calculated using equation 1.56. This equation can be used to estimate the accuracy of the measured BPF and SBRF noise. The Sofasco fan was placed in the lab's anechoic chamber and its' noise spectrum was measured using an Agilent Keysight U8903A audio analyzer. The noise spectrum of the fan when running at the operating voltage is seen in figure 1.13.

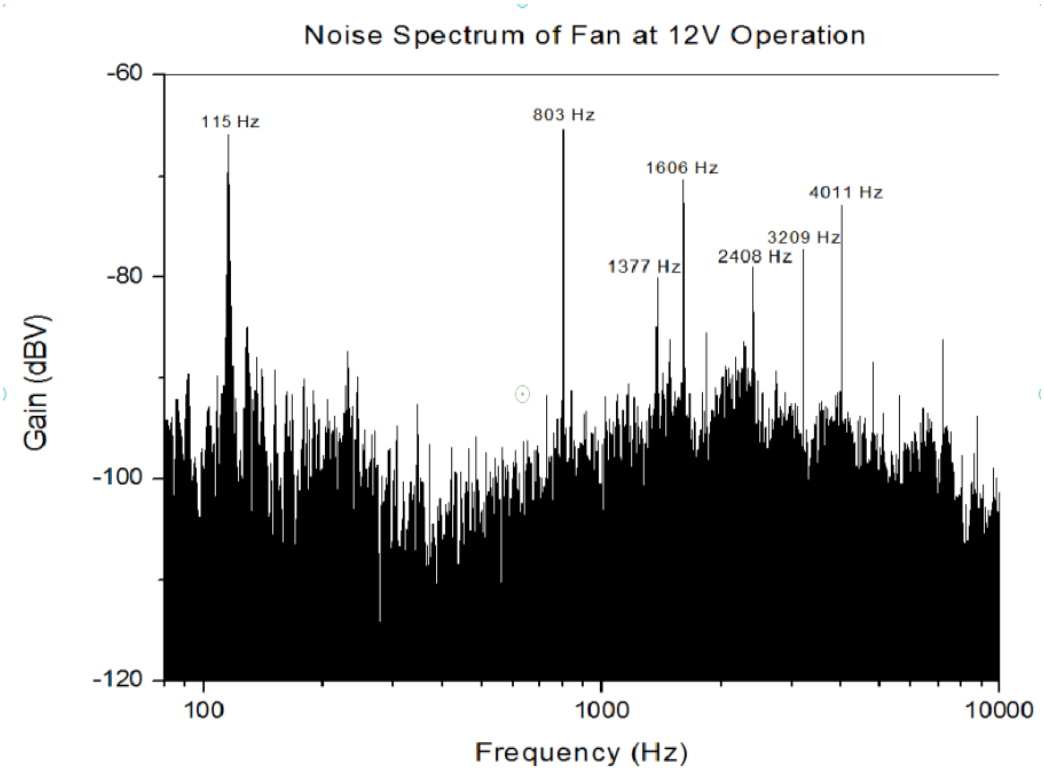

Figure 1.13: In the frequency domain, the figure shows the SPL of the fan at operating voltage (12V).

The single SBRF at 115 Hz, seen in figure 1.13, is such a low frequency that it wouldn't be noticed as much as the higher frequency because humans are not as sensitive to such lower frequencies [5]. The remaining peaks in the frequency spectrum shown in figure 1.13 can be accounted by the BPFs, except for the peak at 1377 Hz. This peak is possibly from a harmonic caused by resonance frequency from the external casing of the fan, but its' exact cause was never determined. Regardless of this peak, by targeting the other six peaks, it would cause a 15 dBV decrease in sound. The frequencies of the measured peaks are compared to the calculated peaks in table 1.3.

Table 1.3: The table lists the first 5 harmonics of the fan's BPF and SBRF.

Peak #	Peak Type	Peak Harmonic #	Measured Frequency [Hz]	Calculated Frequency [Hz]	Percent Error
1	SBRF	1	115	117	-1.71 %
2	BPF	1	803	817	-1.71 %
3	Unknown	N/a	1377	N/a	N/a
4	BPF	2	1606	1634	-1.71 %
5	BPF	3	2408	2451	-1.75 %
6	BPF	4	3209	3268	-1.81 %
2	BPF	5	4011	4085	-1.81 %

The percent error between the measured peaks and the calculated peaks is less than +/- 2 %. The preliminary design of the acoustic metamaterial filter will focus on the BPF first harmonic, which is 35 dBV of the fan noise.

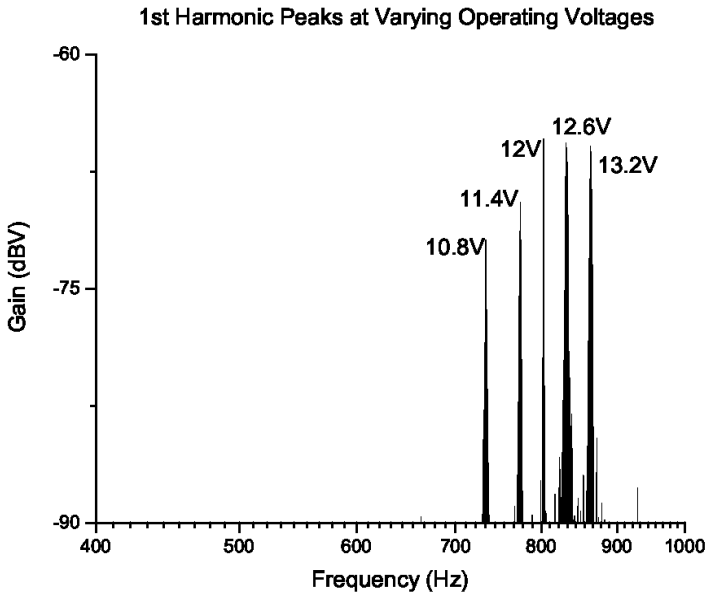

Figure 1.14: In the frequency domain, the figure shows the SPL of the fan's BPF for varying operating voltages.

In figure 1.14, the first harmonic of the BPF at different operating voltages is shown. As the voltage increases, the harmonic of the BPF increases as well. Between 12v and 12.6v, the trend appears to plateau. This trend could be exploited to raise the BPF and thus, allow for smaller resonator cavities. This approach was not explored in the project, due to the potential damage to the fan that could occur when operating outside of 12v. The frequencies of the measured peaks are compared to the calculated peaks in table 1.4 with a percent error of less than +/- 10 % error.

Table 1.4: The table lists the fan's BPF with varying operating voltages.

Percent Difference in Operating Voltage	Voltage [V]	First BPF Measured Frequency [Hz]	First BPF Calculated Frequency [Hz]	Percent Error
-10 %	10.2	734	792	-7.3 %
-5 %	11.4	775	800	-3.1 %
0 %	12.0	803	817	-1.7 %
+5 %	12.6	832	833	-0.1 %
+10 %	13.4	865	841	2.9 %

1.4 Introduction to Design

There are various approaches for creating acoustic metamaterial filters, but there are very few when limiting the restrictions to air flow. The basic approach is to use a resonator to create an acoustic pressure wave that is 180 degrees out phase with the incident wave at the resonance frequency. The created acoustic pressure wave is traveling in the direction opposing the incident wave's direction, which results in destructive interference at the resonance frequency. The destructive interference leads to absorption and/or reflection of the incident wave at the resonance frequency. The papers summarized earlier in this chapter helped the research team determine that

the HR was the type of resonator to use for our design of the acoustic metamaterial. It was also determined, the design of the acoustic metamaterial would try to implement critical coupling technique.

CHAPTER 2: EXPERIMENTS & RESULTS: LARGE SCALE EXPERIMENTS

The purpose of the large scale experiments was to confirm and understand the theoretical equations that govern the HR. The experiments were also used to understand the affects that HRs with different geometries as well as coupled HRs had on the resonance frequency. The structure under test, also known as the sample, is composed of either a single HR or a flow channel with one or more HRs that are attached as side branches. For all the large scale experiments, the flow channel is a piece of PVC pipe and the HR is a Thermofisher Scientific nalgene 50 mL volumetric flask, which is seen in figure 2.1.

Figure 2.1: The volumetric flask used as a HR for the experiments conducted in the lab.

The physical dimensions of the volumetric flask is listed in table 2.1g. The neck length and cavity volume, which are in table 2.1, were determined by physical measurements. The neck length is defined as the length from the top of the flask to where the neck starts to expand and the cavity volume is defined as the remaining volume. The total volume is not the entire volume of the flask but the volume up to a marked point about one-fifths up the neck of the flask, which is a height of approximately 1.6 cm. Therefore, the volume of this section is approximately 2.2 mL and the cavity volume can be estimated by: The physical dimensions of the volumetric flask is

listed in table 2.1g. The neck length and cavity volume, which are in table 2.1, were determined by physical measurements. The neck length is defined as the length from the top of the flask to where the neck starts to expand and the cavity volume is defined as the remaining volume. The total volume is not the entire volume of the flask but the volume up to a marked point about one-fifths up the neck of the flask, which is a height of approximately 1.6 cm. Therefore, the volume of this section is approximately 2.2 mL and the cavity volume can be estimated by:

$$50.00\ [mL] - 2.22\ [mL] = 47.78\ [mL]$$

Table 2.1: The table contains the physical dimensions of the Thermofisher Scientific 50 mL volumetric flask, where some of the dimensions were measured in the lab.

Neck Inner Radius	Neck Length	Total Length	Cavity Volume	Total Volume
0.65 $[cm]$	9.6 $[cm]$	14.6 $[cm]$	47.78 $[mL]$	50 $[mL]$

The amount of water added to the volumetric flask in order to tune it, is calculated by subtracting the desired volume from the original volume of air in the volumetric flask. This is given in equation form as:

$$Water_{Added} = (V_{original}\ [mL] - Vol_{desired}\ [mL]) \cdot \left(\frac{0.999\ [g]}{[mL]}\right) \quad [g] \tag{2.1}$$

where $Water_{Added}$ is the water added to the volumetric flask in grams, using a chemical dropper. The amount of water added to the volumetric flask is verified by using a scale as the water is added with the chemical dropper.

2.1 Experimental Setup

Figure 2.2: The figure is a flow chart of the experimental setup for any large scale experiment.

The experiments performed in the lab had a general experimental setup that is given by the flowchart in figure 2.2. The flowchart details the path of the acoustic wave through the experimental setup, where the measurement is taken inside the EDS Lindgren anechoic chamber. The U8903A audio analyzer generates the test signal that is sent to the Mackie mixer and then, it is sent to the reference monitor inside the anechoic chamber. The U8903A audios analyzer is not controlled by a LabView program unless, there is small region in the frequency sweep that needs a higher resolution. The test structure, or sample, is placed in the anechoic chamber between the reference monitor and the Beyerdynamic MM1 reference microphone. The COMSOL simulations representing the in lab experiments are modeling the anechoic chamber with a perfect matched layer that surrounds the sample setup, which is different for each experiment. The volumetric flask, seen in figure 2.1, which was used as a HR for the in lab experiments, is modeled approximately in the simulations with cylinders for both the neck and cavity.

2.2 Experiment: Single HR With No Flow

Figure 2.3: The physical setup for the single resonator experiment.

The purpose of this experiment was to confirm the predictable behavior of the Helmholtz resonator and the experiment's setup is shown in figure 2.3. This experiment conducted a frequency sweep for two different cavity volumes, which are 0 % and 50% of the cavity's volume, and the resonance frequencies were measured. The measured resonance frequencies were compared to the calculated resonance frequencies to evaluate the predictable behavior of the resonator, which is shown in table 2.2.

Table 2.2: The resonance frequencies of a single resonator with varied volume for both the physical and simulated experiments.

% Water	**Experimental**	**Theory**	**% Error**
0%	169 [Hz]	175 [Hz]	-3.40%
50%	232 [Hz]	248 [Hz]	-6.45%

2.3 Experiment: Single HR As A Side Branch With No Flow

Figure 2.4: The physical setup of the Helmholtz resonator acting as a side branch for the insertion loss measurement. This pipe is positioned in the anechoic chamber for the measurement.

The purpose of this experiment was to confirm the accuracy of the resonance frequency formula for a Helmholtz resonator acting as a side branch. The resonance frequency for a Helmholtz resonator acting as a side branch is the same as the resonance frequency for a Helmholtz resonator not acting as a side branch [2]. The transmission loss due to a side branch can be approximated, but the experiment will not confirm the accuracy of the formula because the experimental setup is for insertion loss [2]. The cavity's volume was varied seven times by adding water to the cavity and the measured resonance frequencies are listed in table 2.3. The calculated and measured resonance frequencies listed in table 2.3 have a maximum error of less than seven percent. The resonance of a HR diverges from the theoretical formula as the volume of the cavity becomes very small because the resonator is closer to a quarter wave resonator (close-ended tube) than a HR. In this experiment, the diverge was not seen in the measured values, but must occur when the cavity is more than 80 percent filled with water.

Table 2.3: The resonance frequencies of a single resonator that is a side branch with varied cavity volumes.

% of water in Cavity	**Theory**	**Measured**	**Simulation**	**Percent Error**
0%	175 [Hz]	187 [Hz]	162 [Hz]	6.85%
20%	196 [Hz]	206 [Hz]	183 [Hz]	5.10%
40%	226 [Hz]	234 [Hz]	211 [Hz]	3.54%
50%	248 [Hz]	254 [Hz]	230 [Hz]	2.42%
60%	277 [Hz]	282 [Hz]	252 [Hz]	1.81%
80%	392 [Hz]	387 [Hz]	349 [Hz]	-1.28%
100%	N/A	459 [Hz]	462 [Hz]	N/A

The COMSOL simulation for this experiment used two cylinders to approximate the shape of the flask. The graph in figure 2.5 shows the results of the COMSOL simulation, but their are significant differences between the simulated and measured values. These difference could be due to the fluid dynamics module being used to model this experiment, which does not acoustic for thermoacoustic effects that occur in the neck of the resonator.

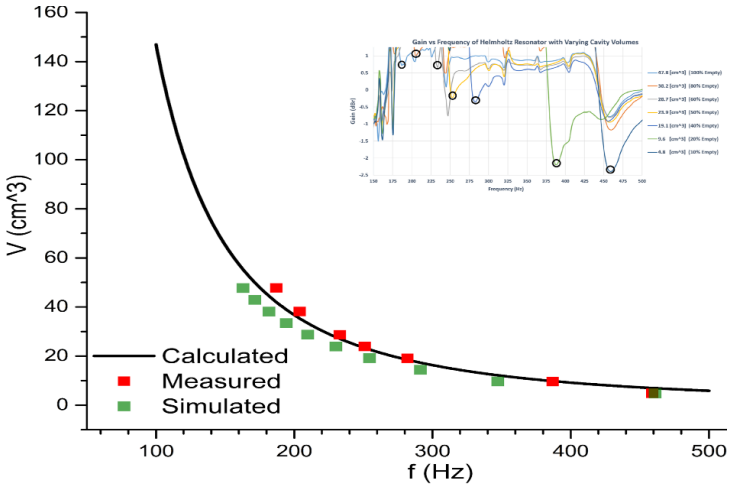

Figure 2.5: The physical results for the insertion loss of a single resonator that is a side branch with varied cavity volumes.

2.4 Experiment: Two Parallel HR As Side Branches With No Flow

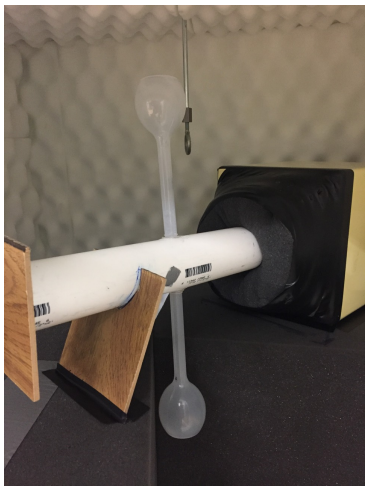

Figure 2.6: The physical experimental setup for the insertion loss experiment of two parallel HRs acting as side branches.

The purpose of this experiment was to confirm the predictable behavior of two parallel HRs acting as side branches and figure 2.6 shows the experimental setup. This experiment is exactly the same as the previous experiment, except their are two HRs. In this experiment, the bottom HR's cavity volume is varied four times, while the top HR has constant volume. A coupling effect can occur when parallel HRs are separated by a small enough distance, which can causes a hybrid resonance for the unit cell containing the HRs [25]. The hybrid resonance is dependent on the resonance of each HR in the unit cell and the hybrid resonance could be shifted from the HR resonance frequency [25]. The results of the experiment are listed in table 2.4 and figure 2.7 shows the difference between the SPL of no sample and the SPL with a sample. The difference in SPL is shown instead the insertion loss because the experiment was not properly set up for measuring the insertion loss. However, the SPL is related to the SWL, which is the measurement used to determine the insertion loss. Therefore, the SPL was used as a rough approximation for the SWL, which shows the resonances, but not the proper loss. The possible coupling effect was

investigated in this experiment, but no coupling effect was not observed.

Table 2.4: The resonance frequencies of a single resonator that is a side branch with varied cavity volumes.

% of water in Cavity	**Theory**	**Measured**	**Simulation**
0%	175 [Hz]	166 [Hz]	168 [Hz]
70%	170 [Hz]	329 [Hz]	303 [Hz]
80%	377 [Hz]	391 [Hz]	364 [Hz]
90%	534 [Hz]	501 [Hz]	477 [Hz]

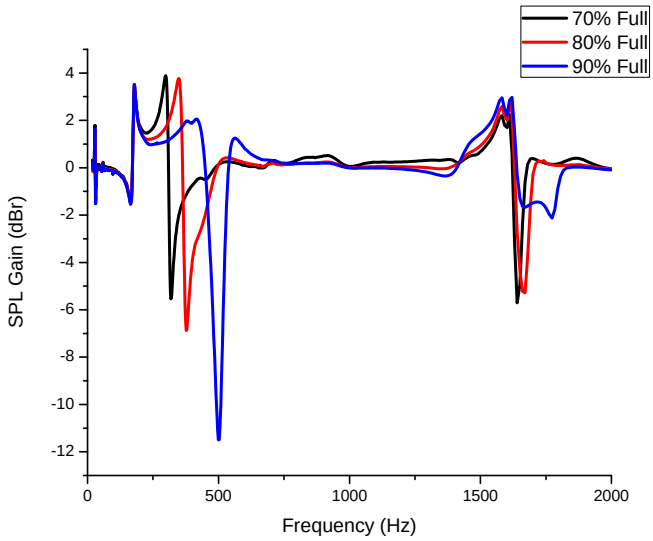

Figure 2.7: The measured results of the difference in SPL for the two parallel HRs acting as a side branch.

CHAPTER 3: SAMPLES AND SAMPLE EXPERIMENTS

The following sections and subsections of this chapter detail the design process and experimental results for the samples designed to reduce fan noise. This design process uses knowledge from the experiments detailed in chapter 2. During the course of the research project, there were four generations of samples that were developed and therefore, the following naming convention will be used throughout the rest of this chapter:

$$S\#\_XX\_LL$$

where S denotes a sample, # denotes the generation of the sample, _ denotes spacing between important indicators, XX denotes the subversion of this sample, and LL denotes with letters, a special subversion. As an example S2_1, denotes the first sample of the second generation.

The samples detailed in this chapter were fabricated with a 3D printer, but not all samples were fabricated with the same 3D printer. The first generation samples were fabricated with Acrylonitrile Butadiene Styrene and they were post processed with acetone to remove the building supports. After the first generation, the samples were created with a Form 2 3D printer, which uses a methacrylate photopolymer liquid resin. The methacrylate photopolymer resign is a proprietary mixer made of methacrylic acid esters, photoinitiators and a proprietary pigment. The Form 2 3D printer has a laser thickness resolution of 0.025 mm and has a laser spot size of 0.14 mm. The samples are post processed with an ethanol and methanol mix, which is used to remove the remaining liquid resin. The post processing mixture is removed from the sample by evaporating the mixing with a high temperature oven. Finally, the sample is cured with an ultraviolet oven.

3.1 Experimental Setup & Hardware

The following subsections describe the hardware and experimental setups used to test the samples described later in the chapter. The first generation samples use the experimental setups from the previous chapter because at the time of the first sample's fabrication and testing, the lab only had the hardware used in the large scale experimental setup. However, the other samples used the hardware and experimental setups described in the following subsections.

3.1.1 Impedance Tubes & Transmission Loss Measurements

The acoustic lab used for testing the samples detailed in this chapter have two different impedance tubes, which are seen in figure 3.1. The SW422 impedance tube has a diameter of 100 mm and the SW477 impedance tube has a diameter of 30 mm. The frequency range of the impedance tube is determined by the diameter of the impedance tube and the length between the microphones.

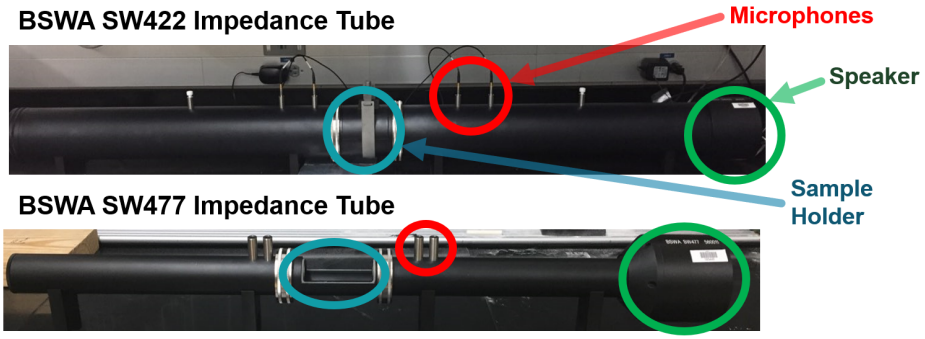

Figure 3.1: The figure is the two impedance tubes that are used in the acoustics lab.

The SW422 impedance tube has a frequency range from 63 Hz to 1600 Hz and the SW477 impedance tub has a frequency range from 1000 Hz to 6100 Hz. Additional information about the BWSA impedance tubes can be found in the product literature manuals [26]. The ISO and ASTM standards are the two main standards used for transmission loss and absorption loss measurements using the an impedance tube. The ISO standard was used for testing the samples because the standard's lack of

difficulty compared to the ASTM standard. Figure 3.2 is a flowchart that details both measurements using the equipment in our lab.

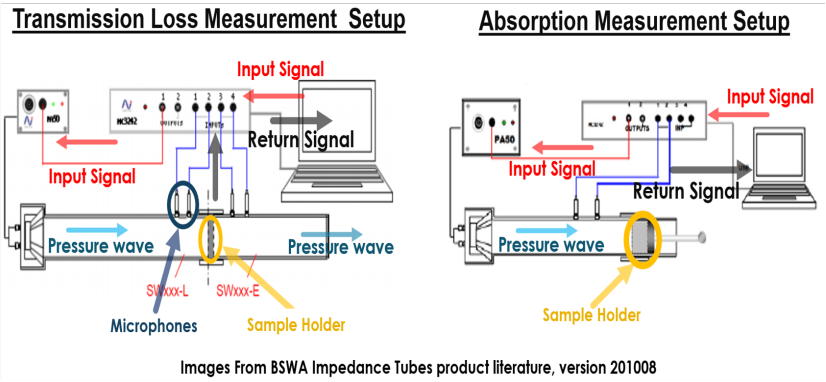

Figure 3.2: The figure shows the flowchart for the transmission loss measurement and absorption measurement using the equipment in the lab.

The impedance tube can be used to determine the reflection coefficient, transmission coefficient, and absorption coefficient using the transfer matrix from scattering matrix theory. As an electrical engineering analogy, the impedance tube can be viewed as a two port system, with the sample acting as the load on the system. Using this analogy, a symmetric and reciprocal system is given by:

$$\begin{bmatrix} p_2 \\ u_2 \end{bmatrix} = \begin{bmatrix} T_{11} & T_{12} \\ T_{21} & T_{22} \end{bmatrix} \begin{bmatrix} p_1 \\ u_1 \end{bmatrix} = \begin{bmatrix} cos(kL) & \frac{jc\rho_0}{S_2} sin(kL) \\ \frac{jS_1}{\rho_0 c} sin(kL) & \frac{S_1}{S_2} cos(kL) \end{bmatrix} \begin{bmatrix} p_1 \\ u_1 \end{bmatrix} \tag{3.1}$$

where p_1 is the pressure at the inlet of the sample in Pa, u_1 is the velocity at the inlet of the sample in m/s, p_2 is the pressure at the outlet in Pa, u_2 is the velocity at the outlet in m/s, k is the wave number in rad/m, ρ is the mass density in kg/m^3, S_1 is the cross sectional of the sample's inlet in m^2, S_2 is the cross sectional of the sample's outlet in m^2, and L is the sample of length in m [21]. Therefore, the transfer matrix is the defined as:

$$TM = \begin{bmatrix} T_{11} & T_{12} \\ T_{21} & T_{22} \end{bmatrix} = \begin{bmatrix} cos(kL) & \frac{jc\rho_0}{S_2} sin(kL) \\ \frac{jS_1}{\rho_0 c} sin(kL) & \frac{S_1}{S_2} cos(kL) \end{bmatrix} \tag{3.2}$$

The software uses the impedance tube measurements to estimate the values of the transfer matrix. The transfer matrix can be used to calculate the reflection coefficient and transmission coefficient can be determined using equations 1.72 and 1.73. The transmission loss is determined using the transmission coefficient by equation 1.80

$$TL\left(\omega\right) = 10 \cdot log_{10}\left(\frac{W_i}{W_t}\right) = 10 \cdot log_{10}\left(\frac{1}{T\left(\omega\right)}\right) \tag{3.3}$$

where ω is angular frequency in rad/s, W_i is the incident sound power in Pa, W_t is the transmitted sound power in Pa, and T is the transmission coefficient. An empty SW477 impedance tube can be represented using equation 3.1 as:

$$\begin{bmatrix} p_2 \\ u_2 \end{bmatrix} = \begin{bmatrix} T_{11} & T_{12} \\ T_{21} & T_{22} \end{bmatrix} \begin{bmatrix} p_1 \\ u_1 \end{bmatrix} = \begin{bmatrix} 1 & 0 \\ 0 & 1 \end{bmatrix} \begin{bmatrix} p_1 \\ u_1 \end{bmatrix} \tag{3.4}$$

The transmission coefficient of an empty SW477 impedance tube can be determined using the transfer matrix from equation 3.4 and equation 1.72 to give:

$$T\left(\omega\right) = \frac{2e^0}{1 + (0)\rho c) + \rho c(0) + 1} = 1 \tag{3.5}$$

The transmission loss for an empty SW477 impedance tube can be calculated using equation 3.5 and equation 1.80 to give:

$$TL(\omega) = 10 \cdot log_{10}\left(\frac{1}{T\left(\omega\right)}\right) = 10 \cdot log_{10}\left(\frac{1}{1}\right) = 10 \cdot log_{10}\left(1\right) = 0 \ dB \tag{3.6}$$

The transmission loss due to no sample in the impedance is given in figure 3.3, which is used as a reference for later measurements.

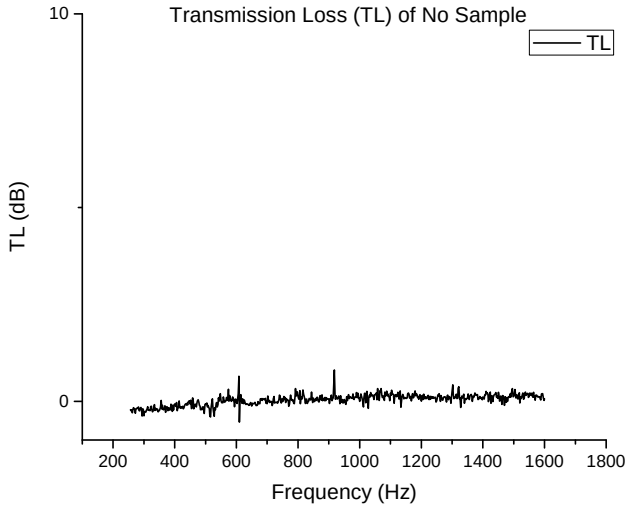

Figure 3.3: The transmission loss of the empty impedance tube.

The results in figure 3.3 show the transmission loss in the empty impedance tube is approximately 0 dB and thus, no transmission loss. The measured results match the predicted transmission loss for an empty SW477 impedance tube using the calculated transfer matrix method.

3.1.2 Insertion Loss Measurements

In acoustics, the transmission loss and insertion loss are used as benchmarks to determine the effectiveness of an acoustic filter. The two measurements can be confusing in the acoustic domain, since they can seem very similar to each other. The insertion loss is defined as the loss due to inserting a device into a system, which is expressed as the ratio of the sound power delivered to the outlet with no sample to the sound power delivered to the outlet with a sample. The transmission loss is defined as the power loss during the transmission over a distance, which is expressed as the ratio of the incident sound power to the transmitted sound power. The major difference between the two measurements is that the transmission loss measurement is independent of the signal's source and the insertion loss is dependent on the signal's

source. The insertion loss and transmission loss are analytically defined as:

$$IL(\omega) = 10 \cdot log_{10}\left(\frac{W_{no}}{W_{sam}}\right) \quad [dB]$$
$$TL(\omega) = 10 \cdot log_{10}\left(\frac{W_i}{W_t}\right) \quad [dB] \tag{3.7}$$

where W_{no} is the sound power at the outlet with no sample in watts, W_{sam} is the sound power at the outlet with a sample in watts, W_i is the incident sound power in watts, W_t is the transmitted sound power in watts, and ω is the angular frequency in rad/s [2]. Using equation 3.7, the insertion loss can be defined in terms of sound pressure level, which is given as

$$IL(\omega) = SWL_1(\omega) - SWL_2(\omega) \quad [dB] \tag{3.8}$$

where ω is the angular frequency is rad/s, SWL_1 is the sound pressure level at the outlet with no sample in dB, and SWL_2 is the sound pressure level at the outlet with a sample in dB [2]. The sound power level is defined as

$$SWL(\omega) = 10 \cdot log_{10}\left(\frac{P(\omega)}{P_{ref}}\right) = L_p(\omega) + 10 \cdot log_{10}\left(\frac{A_s}{A_{ref}}\right) \quad [dB] \tag{3.9}$$

where ω is the angular frequency in rad/s, P_{ref} is the reference sound power in watts, P is the sound power in watts, L_p is the sound pressure level in dB, A_s is the surface area that fully encompasses the source, A_{ref} is reference surface area, which is 1 m^2. The sound pressure level is defined generally as

$$L_p(\omega) = 20 \cdot log_{10}\left(\frac{p(\omega)}{p_{ref}}\right) \quad [dB] \tag{3.10}$$

where p_{ref} is the reference pressure in Pa and $p(\omega)$ is the measured root mean square pressure in Pa [2]. The reference pressure is usually 20 micro-pascals, but it can be any value that is useful. The insertion loss measurement was performed using the impedance tube with the experimental setup seen in figure 3.4. The experimental

setup measures the sound pressure, but the sound power level is calculated with equation 3.9.

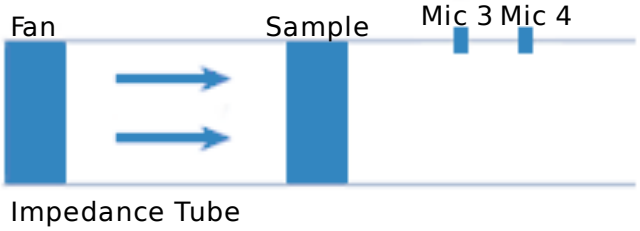

Figure 3.4: The figure shows the setup for insertion loss measurements using the impedance tube.

3.1.3 Airflow Measurement Setup

An important part of the design is not only the transmission and insertion loss, but also the airflow loss due to the acoustic metamaterial. The percent airflow loss is calculated with the following equation

$$\%\, Airflow\, Loss = \left(1 - \frac{AirFlow_{Sample}}{AirFlow_{No\,Sample}}\right) \cdot 100 \tag{3.11}$$

The airflow is measured with a anemometer, which is in figure 3.5. The anemometer is a mechanical device that contains blades, which control a meter that measures the air flow rate. The air flow rate is measured when the air pushes the blades over the course of one minute. This requires the flow through the anemometer to be uniform in order to give an accurate measurement.

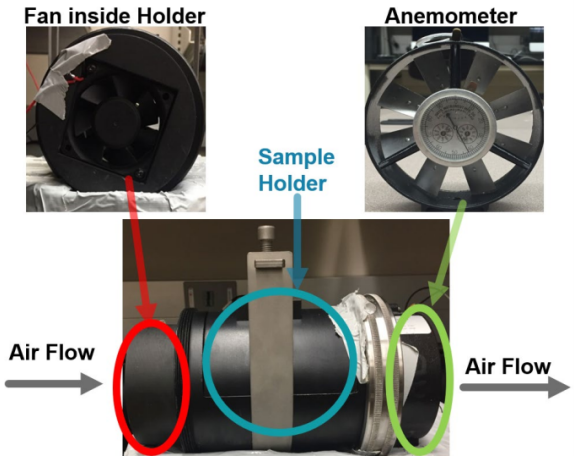

Figure 3.5: The first setup for the airflow experiments.

The airflow measurement setup in figure 3.5 was adjusted because it was determined that there may not be enough time for the airflow to become uniform. In the adjusted airflow measurement setup, the second half of the impedance tube is used along with the sample holder, as seen in figure 3.6. The airflow data seen later in the chapter was measured using the adjusted setup.

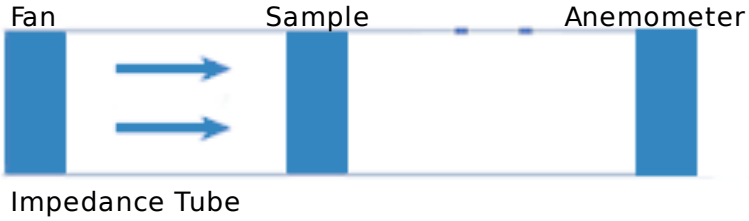

Figure 3.6: The figure shows the setup used for the airflow experiment.

3.2 Samples

The following subsections describe the design process for various samples that were created to attenuate fan noise using insight from the experiments described in chapter 2. These subsections detail various experiments conducted with the samples, but mainly detail the transmission loss and air flow loss of the sample. The transmission loss and air flow loss of the sample are considered the most important factors for a

successfully designed sample, in addition to the size of the sample.

The flowchart seen in figure 3.7 shows the sample development paths, starting with the second generation samples. There are two development paths for the second and third generations, where they focus on the airflow and the transmission loss. The third generation base design is based on the experimental results of the samples from paths 1 and 2. The main measurement for each sample is determined by the sample's development path.

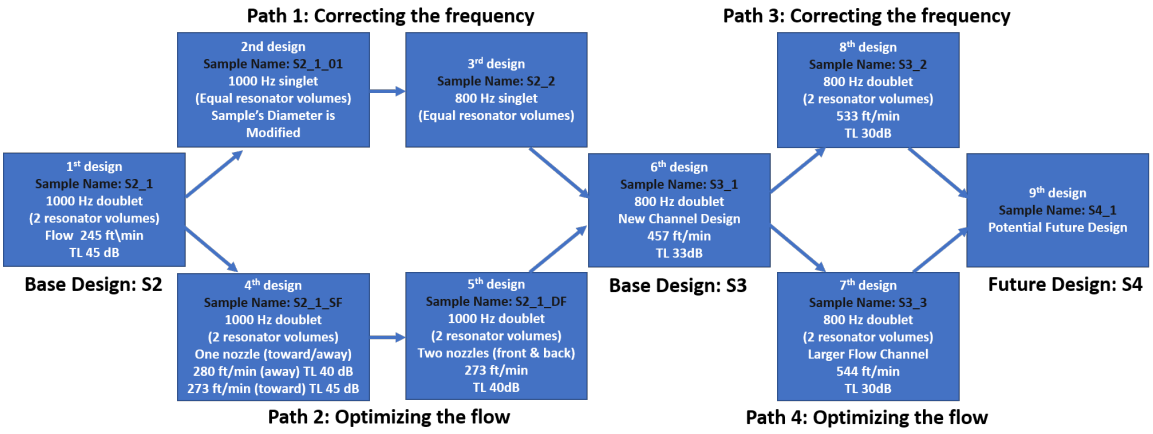

Figure 3.7: The figure shows the evolution of the samples, which are the different design branches.

3.2.1 Sample S1_1

According to Peng and Sheng's paper on metamaterials, two HRs that are side-branches across from each other, as seen in figure 3.8, would produce a hybrid resonance, due to coupling [4].

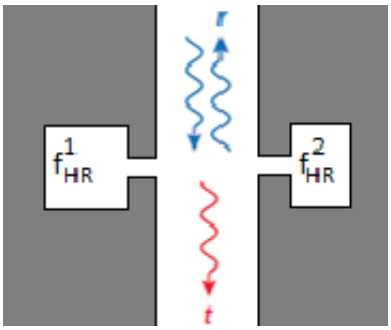

Figure 3.8: The figure shows the layout of the HRs as shown in Peng and Sheng's paper on metamaterials[4].

The hybrid resonance in the paper was stated as:

$$f_{hybrid\ resonance} = \frac{f_{HR2} - f_{HR1}}{2} \tag{3.12}$$

where f_{HR2} is the resonance frequency of the second HR and f_{HR1} is the resonance frequency of the first HR. Using the knowledge from the large scale experiments and the concept from Peng and Sheng's paper, we designed a first generation sample that used higher frequency HRs for targeting lower frequency. The advantage of this approach was to maximize space and increase the number of resonators in the sample. The first generation sample: S1_1 is composed of individual unit cells seen in figure 3.9, which consist of two different HRs. The resonances frequencies of the HRs in the unit cell are 1666 Hz and 3446 Hz. The hybrid resonance according to Peng's paper should be approximately 2556 Hz.

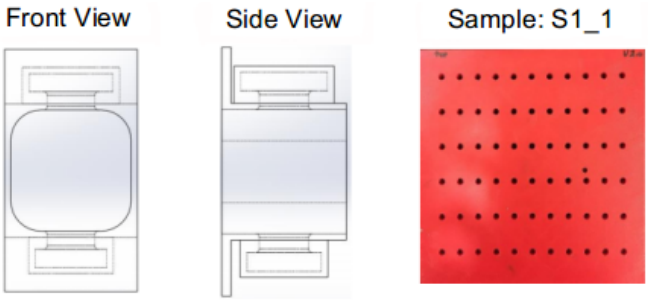

Figure 3.9: The figure shows the unit cells that make up sample: S1_1 as well as sample: S1_1.

The insertion loss for the sample was measured in the anechoic chamber and the results are shown in figure 3.10. These results are considered inconclusive because only one of the resonance frequencies are observable and the reference level is very close to the signal level, which can introduce noise in the insertion loss measurement. The possibility of noise being introduced makes it hard to determine whether small peaks are true peaks or just noise, especially when sounded by many small peaks as seen in figure 3.10. In addition, it was later discovered that there was an error with the hybrid frequency, defined by equation 3.12 and this was confirmed by the author. The correct equation is defined as:

$$f_{hybrid\ resonance} = \frac{f_{HR2} + f_{HR1}}{2} \tag{3.13}$$

Using the corrected formula, the hybrid frequency would be approximately 890 Hz. However, this correction does not change the results being inconclusive and the need for new testing hardware.

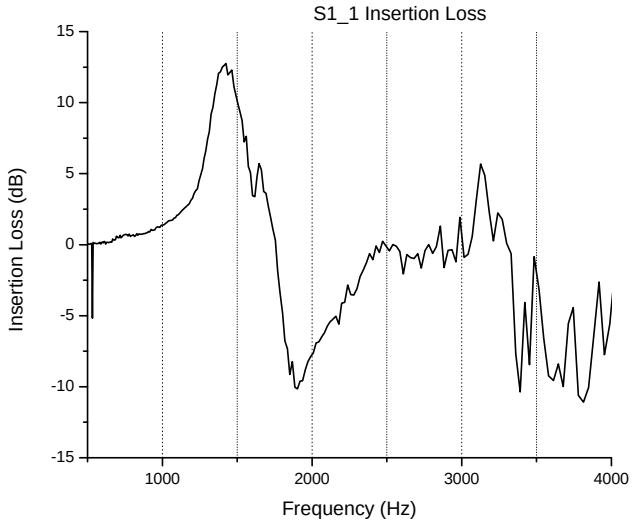

Figure 3.10: The figure shows the insertion loss for sample: S1_1.

3.2.2 Second Generation Sample Design

The first generation sample design consists of rectangular shaped unit cells that were made of two cylindrical HRs and a cylindrical waveguide, as seen in figure 3.9. In each unit cell, there is dead space between the waveguide and the cylindrical HRs that could not be utilized. The geometric form of the sample caused some of the waveguides to be either fully or partially covered by the edge of the fan, which renders the unit cell useless and creates wasted space.

The base design of second generation samples focused on maximizing the number of unit cells by minimizing the dead space and changing the geometric form of the sample to minimize wasted space. The sample's geometric form was changed to be cylindrical because the fan's geometric form is cylindrical and the sample holder's geometric form is cylindrical. The base design has 12 identical unit cells, which are sector shaped and placed every 30 degrees. An additional unit cell, that is not identical to the others, is placed in the middle of the cylinder, as shown in figure 3.11. Therefore, the base design contains 13 unit cells, where each unit cell is made of two identical parallel HRs side branched to a waveguide. The waveguide in each unit cell is a cylindrical tube that is open on both ends and therefore, it is classified as a half wavelength acoustic resonator. The resonance of a half wavelength resonator is calculated with

$$f_n = \frac{n \cdot c}{2 \cdot L} = \frac{n \cdot c}{\lambda} \quad [Hz] \tag{3.14}$$

where c is the speed of sound in m/s, L is the length of the waveguide in m, and n is the harmonic number. The cut-off frequency of a cylindrical waveguide is given by

$$f_{cut} = \frac{c \cdot j'_{ml}}{2 \cdot \pi \cdot a} \quad [Hz] \tag{3.15}$$

where c is the speed of sound in m/s, a is the radius of the waveguide in m, and j'_{ml} the zero of the Bessel derivative function. Under the cut-off frequency, the wave is an

evanescent standing wave (non-propagating wave) that attenuates exponentially.

The waveguides have a diameter of 9 mm and the sample has a diameter of 50 mm. The upper(outer) HR has approximately the same surface area and thus, volume as the lower(inner) resonator as well as the center(middle) resonators. Therefore, the resonance frequency of all three resonators is approximately the same. The second generation base design is shown in figure 3.11, and the HRs are shown highlighted in green. The 3D printed version of figure 3.11 is shown in figure 3.12.

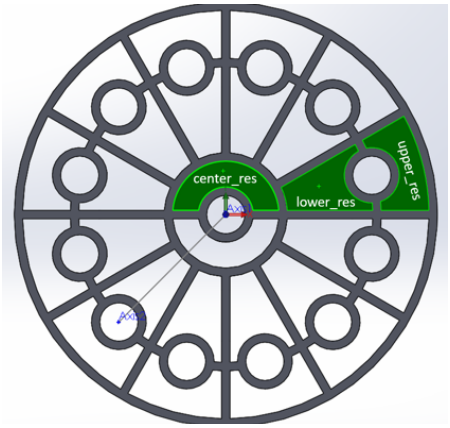

Figure 3.11: The figure shows the base design for all second generation designs, where the sample has a upper (outer) resonator, a lower (inner), and a center (middle) resonator.

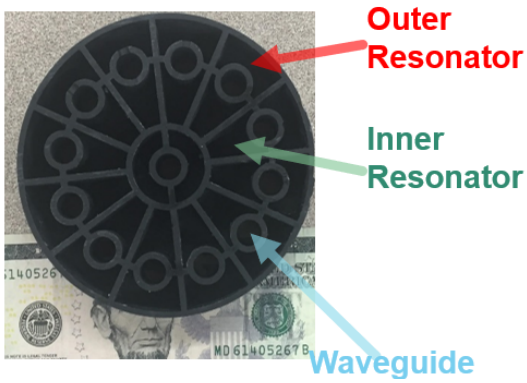

Figure 3.12: The figure shows the inside of a 3D printed second generation sample using a five dollar bill as a reference.

The unit cell's design was based on Peng's paper, which stated the unit cell's resonance was the hybrid resonance frequency. As previously stated, the hybrid

resonance frequency was incorrectly defined in the paper, but this does not have an adverse effect on the design. The correct hybrid resonance frequency is the average of resonance frequencies of the two HR in the unit cell. The resonance frequencies of the two HR are designed to be approximately the same, in order to create a hybrid resonance at that resonance, but has a higher amount of transmission loss. This approach allows for maximizing the available space as well as maximizing the transmission loss. According to Peng's paper, the resonator's in the unit cells act in a coupled manner, similar to a two spring coupled mass system. The upper resonator was designed to be coupled with the lower resonator and the two center resonators are designed to coupled with each other.

3.2.3 Sample: S2_1_Blank

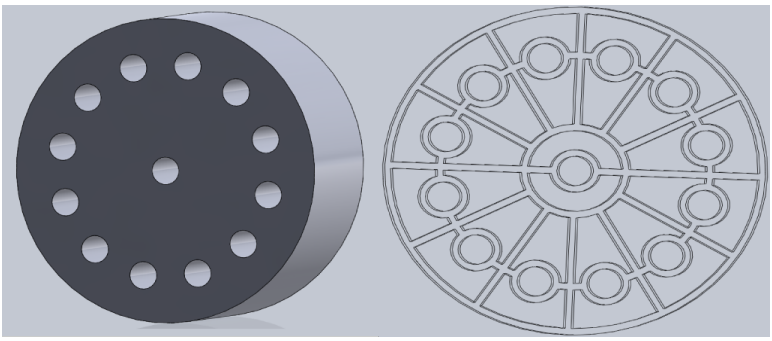

Figure 3.13: The CAD design of the S2_1_Blank sample.

The base design for the second generation samples contains 13 unit cells, where each unit cell is made up of two parallel HRs that are side branched to the waveguide. The blank sample was created to determine the transmission loss due to unit cells with only the waveguides. In order to achieve this, the sample's design is based on the second generation base design, but the necks of the HRs are filled, which is seen in figure 3.13. Therefore, the blank sample's resonance is due to the thirteen waveguides and not the HRs. Using equation 3.14, the resonance of the waveguide with a length (depth) of 50 mm and thus, its' fundamental resonance frequency is 3430 Hz. The

waveguide's cut-off frequency is approximately 30 kHz for the (1,1) mode, which was calculated with equation 3.15.

The measured transmission loss matches closely with the transmission loss from the COMSOL simulation through the frequencies of interest, which is seen in figures 3.14 and 3.15. A potential divergence between the measured and simulated results occurs after 1200 Hz, but this divergence is inconclusive because the measured data may be starting to decrease in transmission loss at 1400 Hz. However, this was not confirmed because the impedance tube's limited testing range, which would require a redesign of the sample for the smaller impedance tube. In addition, the divergence could be caused by the COMSOL simulation not being setup properly or requiring more accurate material properties.

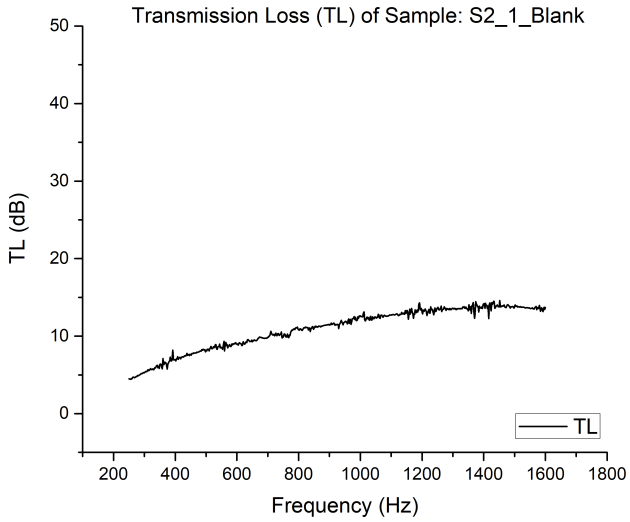

Figure 3.14: The transmission loss of the sample S2_1_Blank from 250 Hz to 1600 Hz.

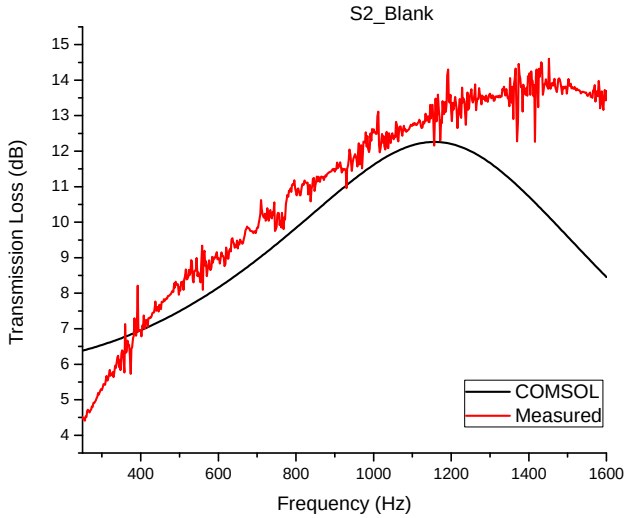

Figure 3.15: The transmission loss of the S2_1_Blank sample from the COMSOL simulations.

3.2.4 Sample: S2_1

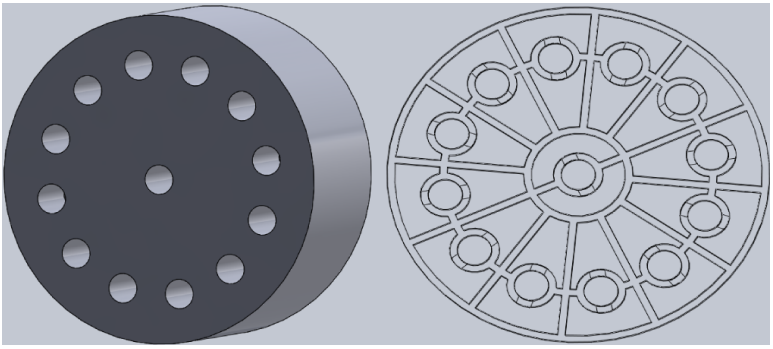

Figure 3.16: The CAD design of sample S2_1.

As stated in a previous section, the base design for every second generation sample contains 12 identical unit cells that are placed every 30 degrees, which creates a cylinder. An additional unit cell, that is not identical to the others, is placed in the middle of the cylinder as shown in figure 3.16. Therefore, every second generation sample contains 13 units cells, which are made of two identical parallel HRs side branched to a waveguide. The two HRs are denoted as the inner HR and the outer

HR based on their location to the waveguide within the unit cell. Every unit cell is designed to attenuate noise at the resonance frequency of the unit cell, which is found by setting the transmission coefficient from equation ... to zero and solving for the angular frequency. The first sample of the second generation design has 13 unit cells designed to attenuated noise at 1000 Hz. This frequency was chosen instead of the fan frequency of 800 Hz because a higher resonance frequency requires a smaller resonator and thus, less material needed for fabrication of the sample. The HRs contained in each unit cell are designed to have a resonance at the target frequency of 1000 Hz. The measured transmission loss was observed to have two peaks at approximately 976 Hz and 1006 Hz, which is seen in figure 3.17. The additional resonance frequency at approximately 976 Hz was not predicted by the design calculations, but the COMSOL simulation confirms the measured results, which is seen in figure 3.17.

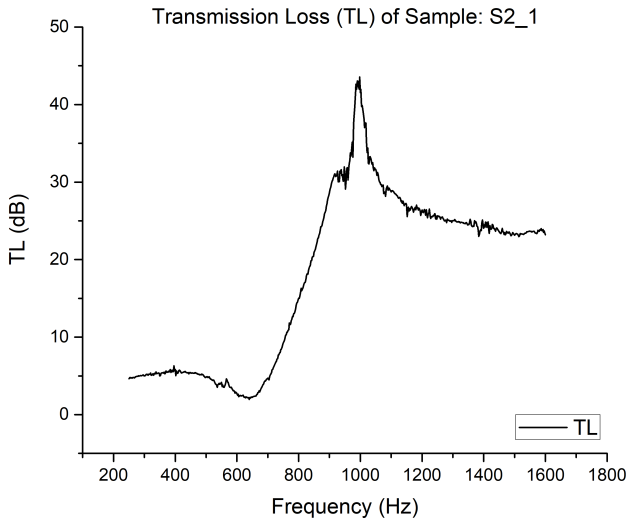

Figure 3.17: The measured transmission loss of the sample S2_1.

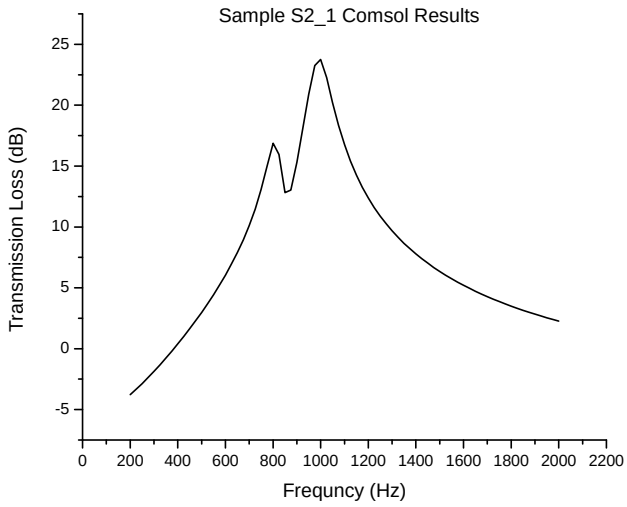

Figure 3.18: The results of the COMSOL simulation for sample S2_1.

The extra resonance peak was due to an error in the CAD design, which caused the HRs in the unit cells to have different cavity volumes and thus, different resonance frequencies. The difference in cavity volumes were caused by differences in the surface areas of the HRs. However, it is important to note that the surface areas of the HRs should be slightly different, because only a unit cell without the waveguide will have exactly the same surface area. The measured and simulated resonance frequencies for each HR in the unit cell are listed in:

Table 3.1: Resonance Frequencies for Sample S2_1

	Calculated Resonance	**Measured Resonance**	**COMSOL Resonance**
Inner HR	1000 $[Hz]$	1006 $[Hz]$	1000 $[Hz]$
Outer HR	952 $[Hz]$	976 $[Hz]$	825 $[Hz]$

The transmission loss of the sample could be affected by the orientation in the impedance tube and therefore, different orientations were tested, which is shown in figure 3.19. The orientation of the sample at zero degrees occurs when the middle of

a waveguide is aligned with the the middle of the impedance tube.

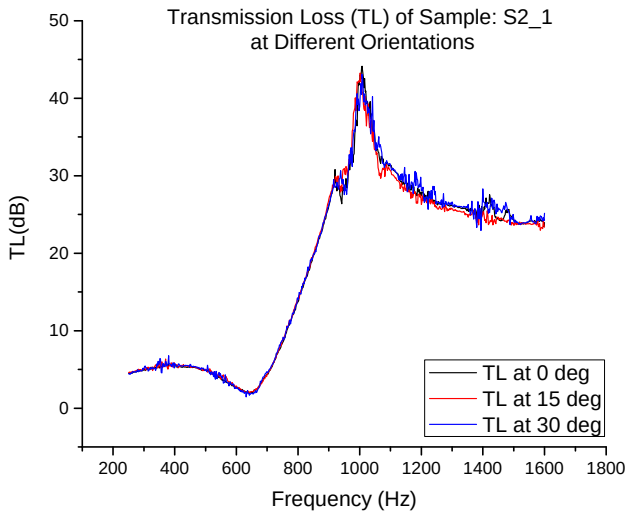

Figure 3.19: The transmission loss of sample S2_1 from 250 Hz to 1600 Hz at different orientations.

The fifteen degree orientation occurs when the sample is rotated to left from the zero degree orientation, which occurs between two waveguides. Similarly, the thirty degree orientation occurs when the sample has been rotated to the left from the zero orientation by thirty degrees. There is no significant difference in the transmission loss between different orientations, which is seen in figure 3.19.

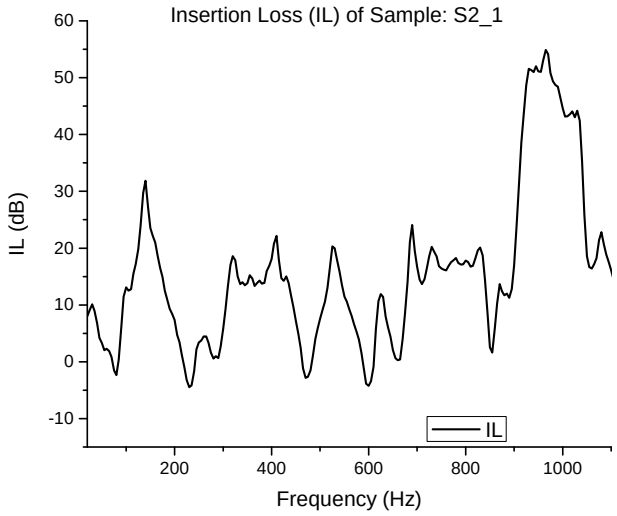

Figure 3.20: The measured insertion loss of the sample S2_1 from 0 Hz to 1100 Hz.

The insertion loss was measured using the experimental setup discussed in section 3.1.2 and the results are shown in figure 3.20. There is an expected noise reduction near or at the resonance frequency of the unit cell, which is seen in the figure. The measured insertion loss is negative at some frequencies, but this is not because there is gain due to the sample. This could be caused by the imperfect experimental setup or extreme changes in background noise around the experimental setup.

The airflow was measured using the experimental setup discussed in section 3.1.3 and the results are shown in figure 3.21. The airflow measurement was taken for various operating voltages in order to determine the characteristics of the fan. The sample's airflow is approximately 245 ft/min at the fan's recommended operating voltage of 12 volts, which is shown in figure 3.21. The airflow loss at the fan's recommended operating voltage of 12 volts is 74.5 percent.

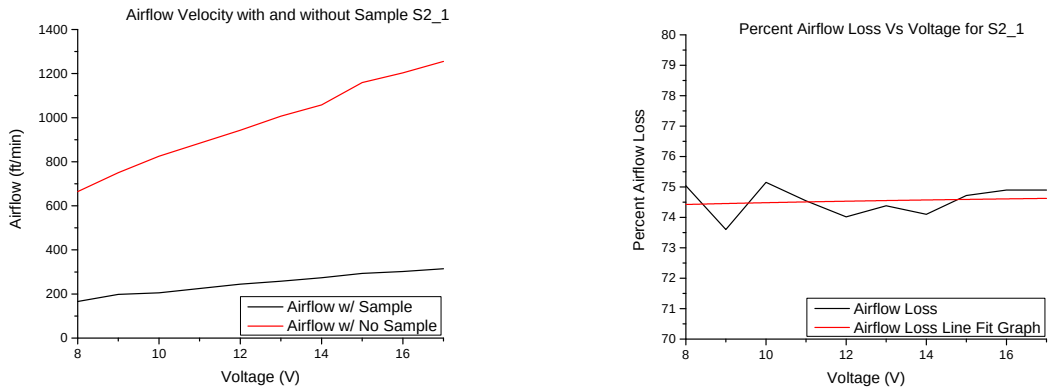

Figure 3.21: The airflow and airflow loss of the sample S2_1.

3.2.5 Sample: S2_1_SF

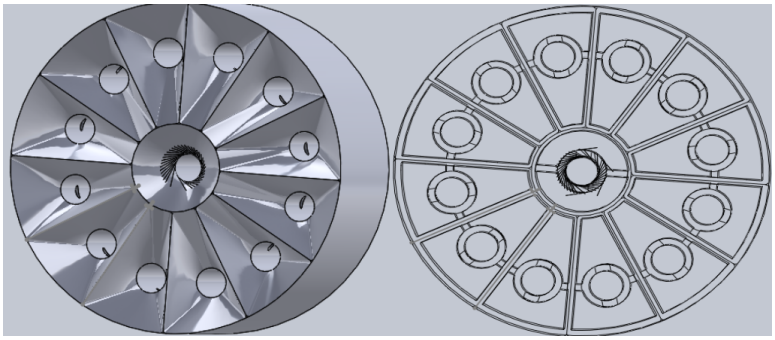

Figure 3.22: The CAD design of sample S2_1_SF.

The design for S2_1_SF was based on trying to improve the airflow of the S2_1 design by adding a nozzle to the outlet of the S2_1 sample. The nozzle was added to outlet in order to increase airflow by reducing drag. This design is called a diverging nozzle, where the waveguide acts as the nozzle's throat. The nozzle improved the airflow by approximately 3 percent, which is seen in figure 3.23. However, this improvement was not significant enough to justify the increase in sample size and the increase in material used to create the sample.

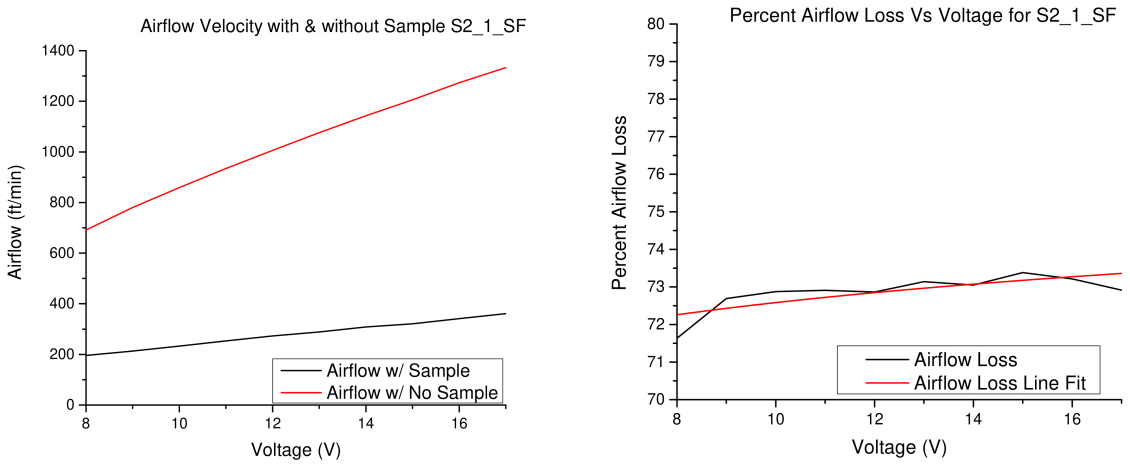

Figure 3.23: The airflow and airflow loss of the sample S2_1_SF.

The sample was designed to have a resonance frequency of 1000 Hz and the measured resonance frequency is 938 Hz. The transmission loss for the sample is shown in figure 3.24 and the figure shows the transmission loss for both possible orientations of the sample.

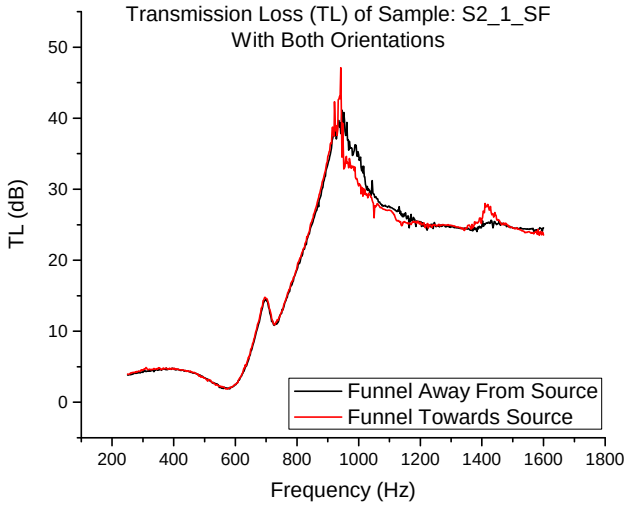

Figure 3.24: The transmission loss of the sample S2_1_SF from 250 Hz to 1600 Hz for different orientations.

3.2.6 Sample: S2_1_DF

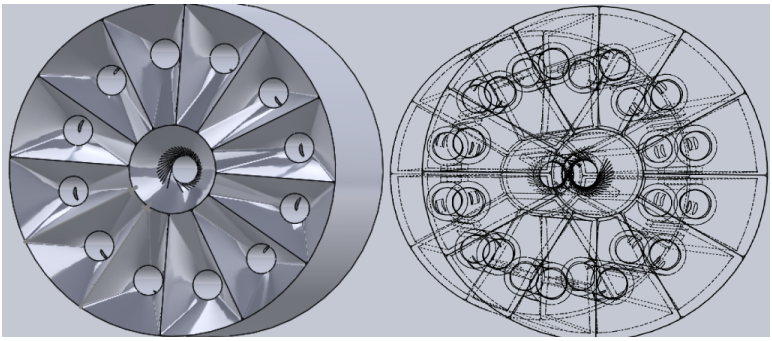

Figure 3.25: The CAD design of sample S2_1_DF.

The design for S2_1_DF is a extension of the design for S2_1_SF with a nozzle on each side and the sample design is shown in figure 3.25. The additional nozzle was added to the sample because it was thought it would reduce drag and increase velocity of the air. This design creates a converging-diverging nozzle, where the waveguide acts as the throat of the nozzle. The converging-diverging nozzle setup allows for either supersonic or subsonic airflow from the outlet. In addition, when the throat of the nozzle is choked then the mach number in the throat is one [6]. The air density in the throat is approximately 60 percent of the original air density outside the sample, when the mach number is one [6]. In the case the of the nozzle not being considered choked, the air density in the throat is approximately 50 percent of the density outside the sample [6]. The sample was designed to have a resonance frequency at 1000 Hz, but if the nozzle is chocked the resonance frequency is shifted to approximately 1300 Hz. This resonance frequency shift occurs because the speed of sound in the throat is approximately 445 m/s due to the difference in air density in the throat. The transmission loss of the sample shown in figure 3.26 is approximately 1300 Hz, which means the mach number in the throat is one.

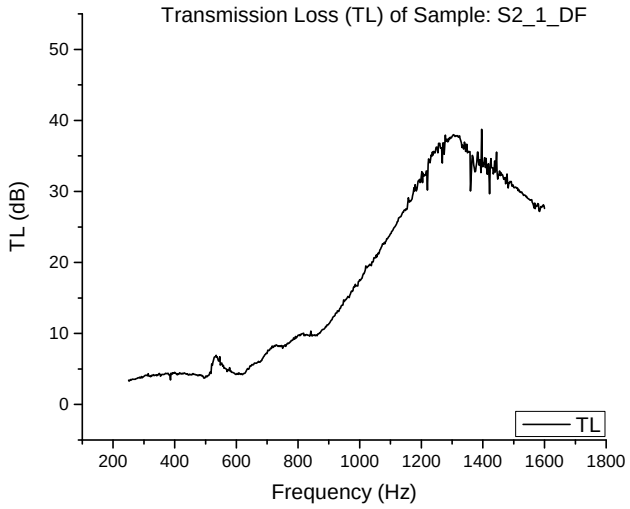

Figure 3.26: The transmission loss of the sample S2_1_DF from 250 Hz to 1600 Hz.

The airflow at the inlet of the nozzle is 1200 ft/min and is a subsonic flow because the mach number is 0.017, which is less than one. As seen in figure 3.27, the converging-diverging nozzle did not succeed in creating a sonic or supersonic flow at the outlet. It marginally improved the airflow loss over the original sample, but it is not worth the added material for the small trade off and the reduction in the transmission loss.

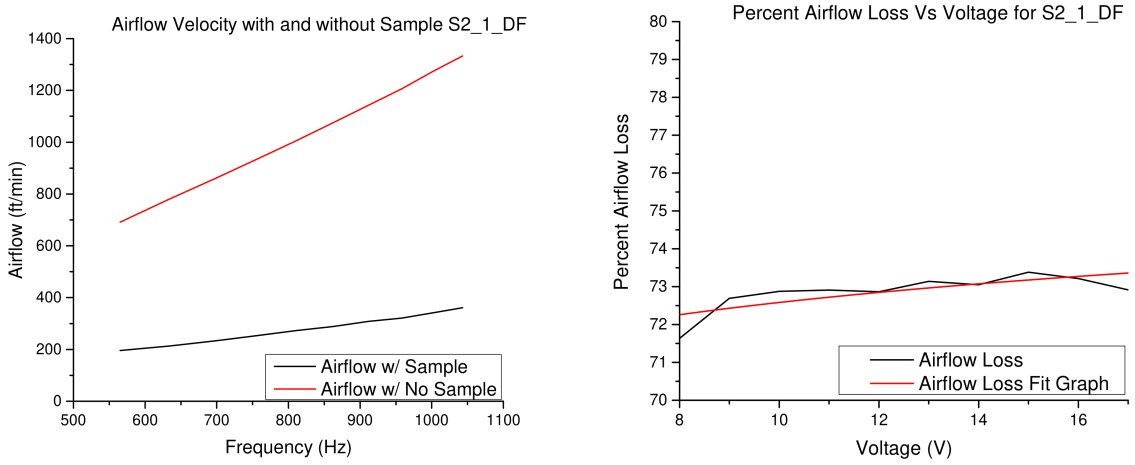

Figure 3.27: The airflow and airflow loss of the sample S2_1_DF.

After the design process and fabrication, it was discovered that the airflow at the

outlet of the nozzle is controlled by a ratio in the surface areas, which is given by:

$$\frac{A^*}{A_e} = M_e \left(\frac{\frac{\gamma+1}{2}}{1 + \left(\frac{\gamma-1}{2} \cdot M_e^2 \right)} \right)^{\frac{\gamma+1}{2\,(\gamma-1)}} \tag{3.16}$$

where A_e is the surface area of at the exit in m^2, A^* is the surface area of the throat in m^2, M_e is the mach number at the outlet, and γ is the specific heat ratio [6]. The area ratio for the sample is 0.0449 and solving for mach number at the exit gives 0.025, which means the airflow is subsonic as seen in the airflow measurements. The airflow at the outlet is given by the following equation:

$$v_e = \sqrt{\frac{2\ \gamma\ R\ T_t}{\gamma - 1} \left(1 - \frac{1}{1 + \left(\frac{\gamma-1}{2} \cdot M_e^2 \right)} \right)} \quad [\,m/s\,] \tag{3.17}$$

where γ is the specific heat ratio, M_e is the mach number at the exit, R is the specific ideal gas constant in $J/(mol \cdot K)$, and T_t is the temperature in the throat in K [6].

3.2.7 Sample: S2_2

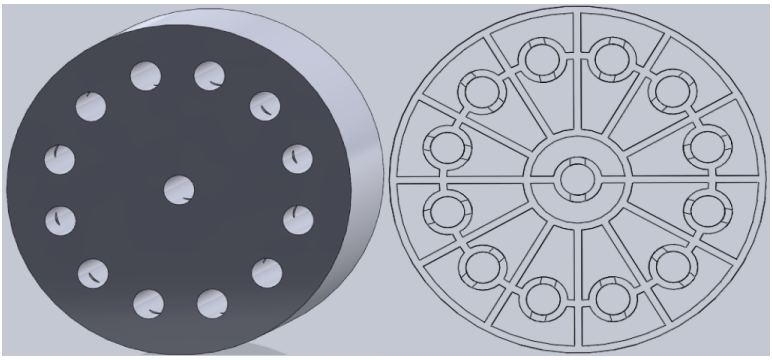

Figure 3.28: The CAD design for sample S2_2.

In the previous samples, the target attenuation frequency of the unit cell was 1000 Hz, but the required target attenuation frequency for the fan is approximately 800 Hz. The previous samples were mainly designed at 1000 Hz to allow for fabricating a smaller sample, which used less materials. In addition, humans perceive the sound

pressure level at 1000 Hz to be greater than at the fan frequency of approximately 800 Hz, which allows for easier human testing of the sample. The purpose of sample S2_2, which is seen in figure 3.28, is to create the same type of attenuation seen in sample S2_1, but with the target attenuation frequency of the fan's fundamental frequency. This was achieved by changing the depth of every resonator to 70 mm, which decreases the resonance to approximately 800 Hz. The CAD design error seen in the previous second generation samples was corrected in this sample and this prevented the noticeable doublet peaks. This was achieved by changing the surface area of the outer, inner, and center resonators to be close to the same value, which is detailed in table 3.2.

Table 3.2: The surface areas and volumes of the resonators for the original design and the adjusted design.

Design	Resonator	Surface Area [mm^2]	Volume [mm^3]
Original Design	Outer	180.22	9011
	Inner	162.26	8113
	Center	160.12	8006
Adjusted Design	Outer	171.17	12496
	Inner	168.86	12667
	Center	169.39	12535

The transmission loss of sample S2_2, seen in figure 3.29, is approximately 45 dB at approximately 800 Hz, which was the target frequency. There is another transmission loss peak at approximately 1450 Hz that is caused by the standing waves in the HR and this is predicted in [5], which is also seen in experiments in chapter 2. The amount of attenuation is similar to that seen in the previous samples, which was the desired outcome of this design.

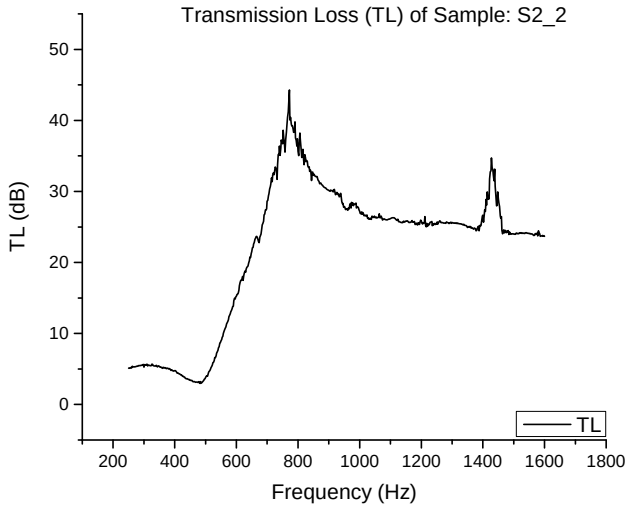

Figure 3.29: The transmission loss of sample S2_2 from 250 Hz to 1600 Hz.

3.2.8 Third Generation Sample Design

The second generation samples obtained ideal transmission loss at the resonance frequency with very low airflow. In order to significantly increase the airflow, the waveguide's shape and size must be optimized to use all available space to increase the waveguide's surface area. The cylindrical waveguides used in the second generation samples wasted space internally on both sides of the waveguide, which can be seen in figure 3.28. The base design for the third generation samples eliminates the wasted space caused by the cylindrical waveguides by changing the waveguide's shape to a truncated sector, which is shown in figure 3.30. However, there is still a small amount of wasted space where the walls converge at the center of the third generation samples, but all other space has been completely optimized. The design could be optimized further by reducing the wall's thickness, which is 2 mm. The Form 2 3D printer has the printing resolution to print walls less than 2 mm, but structural integrity issues would arise with smaller wall thickness. In addition, there are potential stability issues that could occur during the printing process, which would cause the fabrication process to fail. These problems could potentially be resolved by using a different

material and/or a different type of 3D printer, but this was not explored in the project.

Figure 3.30: The figure is a cross sectional piece of the base design for the third generation samples. The waveguide is the truncated sector that is highlighted in blue.

There is a relationship between the waveguide's surface area and the transmission loss of the sample, which creates a trade-off between the airflow and the transmission loss. The trade-off can analytically be shown by the transmission coefficient for branch parallel HRs, which is given by

$$T_{Coeff}(\omega) = \frac{2 \cdot Z_{HR}(\omega)}{N \cdot Z + 2 \cdot Z_{HR}(\omega)} = \frac{2 \cdot Z_{HR}(\omega)}{N \cdot \frac{\rho \cdot c}{S_{wave}} + 2 \cdot Z_{HR}(\omega)} \tag{3.18}$$

where ω is the angular frequency in rad/s, Z_{HR} is the impedance in ohms of a HR in terms of the angular frequency, N is the number of HRs in parallel with each other, Z is the impedance in ohms of the waveguide, S_{wave} is the surface area of the waveguide in m, ρ is the mass density in kg/m^3, and c is the speed of sound in m/s [25]. Using equation 1.80 and equation 3.18, the transmission loss given in dB is defined as:

$$TL(\omega) = 20 \cdot log_{10}\left(\frac{1}{T_{Coeff}(\omega)}\right) = 20 \cdot log_{10}\left(\frac{N \cdot \frac{\rho \cdot c}{S_{wave}} + 2 \cdot Z_{HR}(\omega)}{2 \cdot Z_{HR}(\omega)}\right) \tag{3.19}$$

The waveguide's surface area, S_{wave}, is defined by:

$$S_{wave} = \left(\frac{r_t^2 \cdot \theta}{2} - \frac{r_{in}^2 \cdot \theta}{2}\right) \; [\, m^2 \,] \tag{3.20}$$

where r_t is the radius of the inner circular sector plus the radius of the waveguide in m, r_{in} is the radius of the inner circular sector in m, and θ is the angle of both circular sectors in radians. As seen in equation 3.19, the transmission loss decreases at a given angular frequency as the waveguide's surface area increases, which causes the trade-off between airflow and transmission loss. The analytical analysis of the trade-off is not true when the impedance of each HR is different, which was not explored in chapter 3.

As a result of using the truncated sector as a waveguide, the volume of the HR decreases and thus, the resonance frequency increases. This effect can be offset by increasing the depth of the HR, which results in the total depth of the sample increasing. Therefore, there is an additional trade-off using this method to increase the airflow, which is an increase in sample depth.

3.2.9 Sample: S3_1

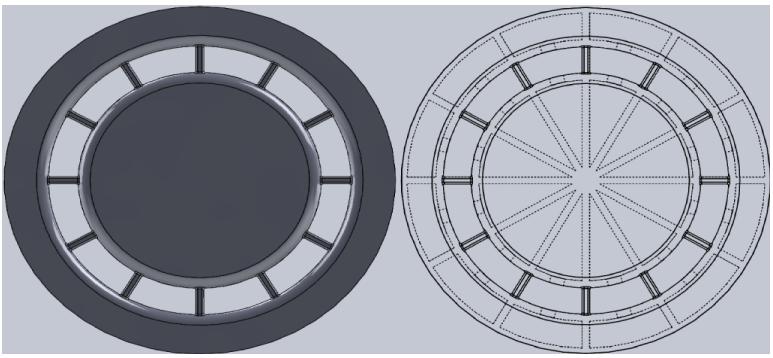

Figure 3.31: The CAD design for sample S3_1.

As stated in the previous section, the base design for every third generation sample is focused on significantly increasing the airflow by optimizing the size and shape of the waveguide, in order to reduce wasted space. This optimization is partially achieved in the base design for every third generation sample by using a truncated sector as the waveguide's shape. Further optimization of third generation samples can be achieved by increasing the waveguide's surface area. The waveguide in the

first sample, seen in figure 3.31, is defined by a truncated sector located between two radii along the unit cell, which is shaped as a sector. The two radii are defined as the radii along a unit cell from sample S2_2, which denotes the location of the outer HR's neck and inner HR's neck. Using equation 3.20, the surface area of the waveguide in sample S3_1 is 121.38 mm^2. The cross-sectional area of the waveguide has increased by approximately 91 percent from the cross-sectional area of waveguide for sample S2_1, which is approximately 63.62 mm^2. The first sample of the third generation design uses the same resonator depth as sample S2_2, which is 70 mm. Therefore, the total depth of sample S3_1 is 74 mm. The resonator depth was chosen to be the same as sample S2_2, in order to simplify the design of the sample. The sample's diameter is 99 mm, which is a decrease of 1 mm from the diameter of any second generation sample. The diameter was decreased to help the sample fit better into the impedance tube's sample holder.

The sample's airflow is approximately 450 ft/min at the fan's recommended operating voltage of 12 volts, which is shown in figure 3.32. The airflow increased by approximately 84 percent from the airflow in sample S2_1, which is 245 ft/min. As shown in figure 3.32, the airflow loss at the fan's recommended operating voltage is approximately 55 percent, which is an approximately 26 percent decrease from the airflow loss for sample S2_1, which is percent.

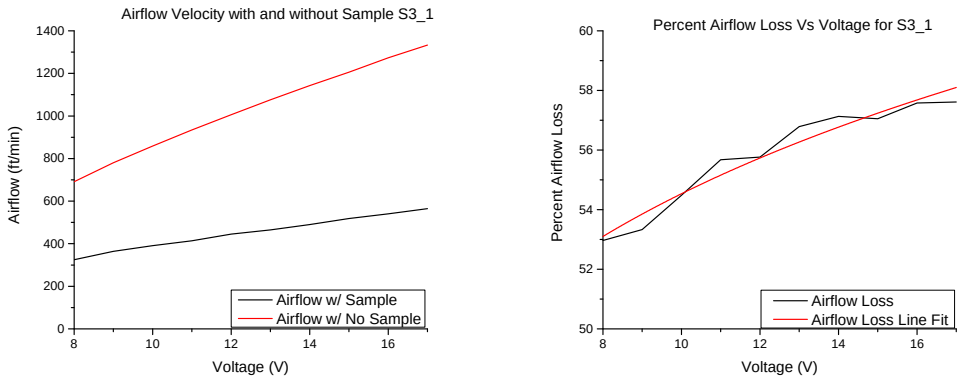

Figure 3.32: The airflow and airflow loss of sample S3_1.

The calculated resonance frequency is 780 Hz and the measured resonance frequency is approximately 790 Hz. The transmission loss of sample S3_1 is 33 dB, which is approximately 15 dB less than sample S2_2. A reduction in transmission loss was predicted by equation 3.19, due to the increase in the waveguide's cross-sectional area. The reduction in transmission loss is also caused by the unit cells being reduced from 13 to 12 in third generation samples.

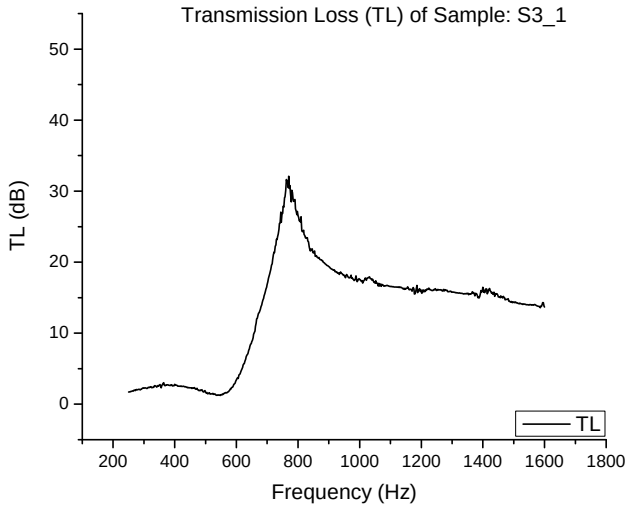

Figure 3.33: The measured transmission loss of sample S3_1 from 250 Hz to 1600 Hz, with a resonance at 790 Hz.

3.2.10 Sample: S3_3

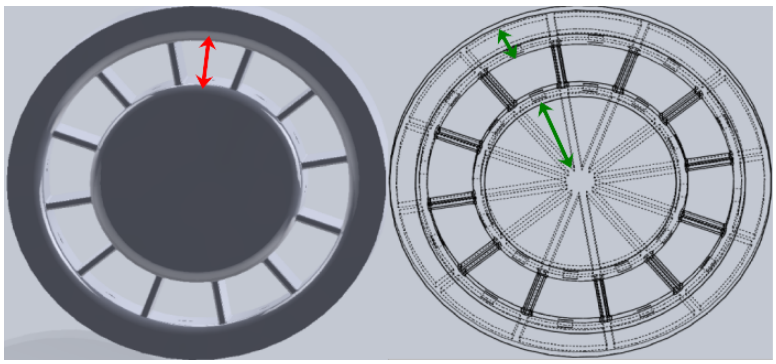

Figure 3.34: The CAD design for sample S3_3. The red arrow indicates how the waveguide's surface area will increase. The green arrows show how the resonators' surface area will decrease.

The design of sample S3_3 focused on decreasing the airflow loss, while limiting the decrease in transmission loss. The airflow loss was decreased by increasing the surface area of the waveguides, while decreasing the surface area of the resonators. This is shown in figure 3.34, where the red arrow indicates the increase in the waveguide's height, which indicates the increase in the waveguide's surface area. The green arrows show the decrease in the height of the resonators, which shows the decrease in the surface area of the resonators.

As previously stated, this approach to decreasing the airflow loss has various trade-offs, such as, the decrease in transmission loss with the increase in the waveguide's surface area. An additional trade-off for this method is the required increase in the resonators' depth in order to keep the same resonance frequency. The depth of the resonators were increased by 15 mm to 85 mm compared to the depth of the resonators in sample S3_1, which is 70 mm. The required increase in the resonators' depth increases the total depth of the sample, which is the true additional trade-off with the increase in the waveguide's surface area. The depth of the sample was increased by 15 mm to 89 mm compared to the total depth of sample S3_1, which is 74 mm. The importance of this trade-off is dependent on the application of the

sample in terms of the maximum size of the sample.

The cross-sectional area or surface area of the waveguide is calculated with equation 3.20. Therefore, the waveguide's surface area for sample S3_3 is approximately 188 mm^2. The waveguide's surface area increased by 195 percent from the waveguide's surface area in sample S2_1, which is 63 mm^2. In addition, the waveguide's surface area increased by 55.37 percent from the waveguide's surface in sample S3_1, which is 121 mm^2.

The transmission loss of the sample at the resonance frequency of 800 Hz is approximately 30 dB, which is shown in figure 3.35. As previously discussed in this section, the transmission loss was expected to decrease with an increase in the surface area of the waveguide. The transmission loss decreased by approximately 3 dB from the transmission loss of sample S3_1, which was approximately 33 dB. Therefore, the trade-off for a 55.37 percent increase in surface area is a decrease of 3 dB in transmission loss.

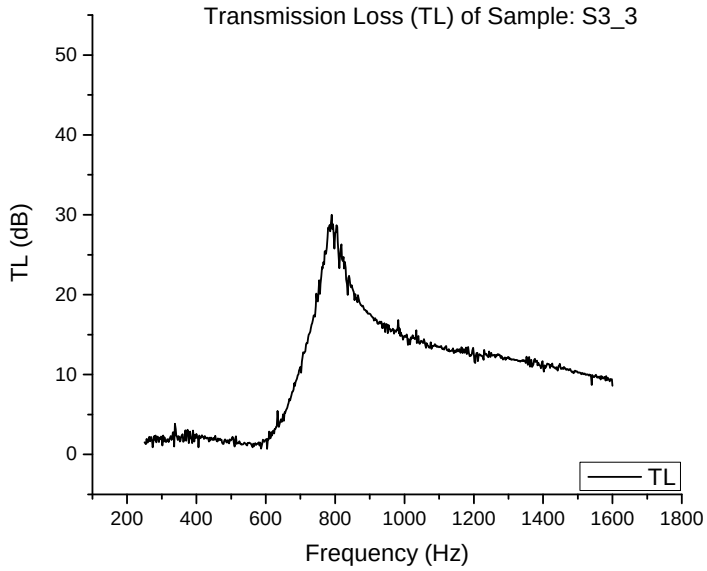

Figure 3.35: The measured transmission loss of sample S3_3 from 250 Hz to 1600 Hz, with a resonance at 800 Hz.

The sample's airflow is approximately 544 ft/min at the fan's recommended operating voltage of 12 volts, which is shown in figure 3.36. The airflow increased by approximately 123 percent from the airflow in sample S2_1, which is 245 ft/min. In addition, the airflow increased by approximately 21 percent from the airflow in sample S3_1, which is 450 ft/min. As shown in figure 3.36, the airflow loss at the fan's recommended operating voltage is approximately 45.5 percent, which is an approximately 39 percent decrease from the airflow loss for sample S2_1. The airflow loss decreased by approximately 17 percent from the airflow loss for sample S3_1, which is 55 percent.

The waveguide's surface area was increased by 55.37 percent, which resulted in the airflow increasing by approximately 21 percent and the airflow loss decreased by 17 percent, with a trade-off of approximately 3 dB in transmission loss at the resonance frequency.

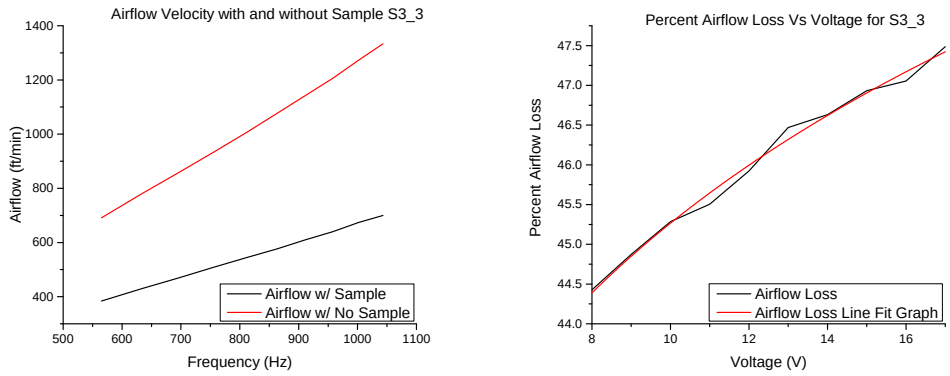

Figure 3.36: The airflow and airflow loss of the sample S3_3.

CHAPTER 4: CONCLUSIONS

Every sample from chapter 3 has advantages and disadvantages, but none of them are superior over the other. There is a trade-off between the airflow and the transmission loss, which shown by the results of the second and third generation samples. The trade-off can analytically be shown by the transmission coefficient for branch parallel HRs, which is given in equation 3.18. As seen in equation 3.19, the transmission loss decreases as the transmission coefficient increases. The transmission loss decreases as the cross-sectional area of the waveguide increases, which causes the trade-off between airflow and transmission loss. The analytical analysis of the trade-off may not be true when the impedance of each HR is different, which was not explored in chapter 3. This could be explored by expanding equation 3.19 accordingly. These trade-offs could be negated by accounting for the decrease in the characteristic impedance of the waveguide, which is due to the increase in the cross-sectional area of waveguide. This could be achieved by increasing the mass density and speed of sound to account for the increase in cross-sectional area. In addition, other losses, such as, thermo-acoustic losses could be introduced into the waveguide to increase the impedance. However, those methods were not explored in this project due to time constraints. These trade-offs would also be negated by treating our metamaterial as one unit cell and then, combining N unit cells in series. This was shown to dramatically increase the transmission loss in the Silencer paper. However, this would introduce the trade-off of increasing the material and depth of the metamaterial.

The second generation sample with double funnels shifted the resonance by 300 Hz and the sample with a single funnel shifted the resonance down by approximately 65 Hz. In addition, the single funnel had a satellite peak at around 750 Hz with TL of

approximately 15 dB. The cause of the shifting effects were explained in chapter 3, but they were not exploited for later designs. These effects could be further explored and exploited with a design that allows more airflow than our funnel samples. In addition, this could be combined with the broadband filter mentioned below, to achieve interesting shifting effects.

The samples from chapter 3 are narrow stop-band filters or notch filters and their frequency range is controlled by the resonance frequency and Q-factor. The Q-factor controls the bandwidth of the filter and the resonance frequency is the location of maximum transmission loss. The resonance frequency is controlled primarily by the physical dimensions of the sample, which were not tunable for samples in chapter 3. These samples would be more practical for real world use with a tuning mechanism, which allowed the resonance frequency to be adjusted over a select frequency range. This could be achieved by creating samples with an elastic material and tuning it by compressing the sample. The compression of the sample could be held in place with a brace that could manually adjusted. The resonance frequency would shift to a higher frequency as the sample is compressed because the cavity of the HR is reduced. This method as well as others could be explored to achieve a tuning mechanism for the samples. This method was briefly explored in the project, but complications due to post-processing as well as time constraints prevented further exploration. This also prevented experiments exploring HRs with elastic cavity back walls, which lowers the resonance frequency.

The airflow produced by the fan increases as the fan's RPM increases, but the airflow out of the samples do not increase at the same rate, which is shown in the sample's airflow velocity graphs. This eliminates the ability to just increase the fan's voltage to increase airflow.

Overall, the second generation samples have a better transmission loss and the third generation samples have significantly better airflow. The application of the sample

would dictate the most important trade-off parameter and thus, the best sample to use. As an example, the correct sample to use for maximum airflow would be sample S3_3 and the correct sample to use for maximum transmission loss would be sample S2_1.

A broadband acoustic metamaterial can be designed using the results from chapter 2 and 3. The shifting effects due to coupling two parallel HRs are never realized in the previous designs due to the space between the HRs. These coupling effects can be forced by reducing the distance between the resonators to zero. This is achieved by connecting the two HRs to each other on the outer edge of the sample. Figure 4.1 and 4.2 show two different CAD designs for a broadband acoustic metamaterial. The inner HR acts as a pumping mechanism for the outer HR and the direction of flow into the outer HR is dependent on frequency.

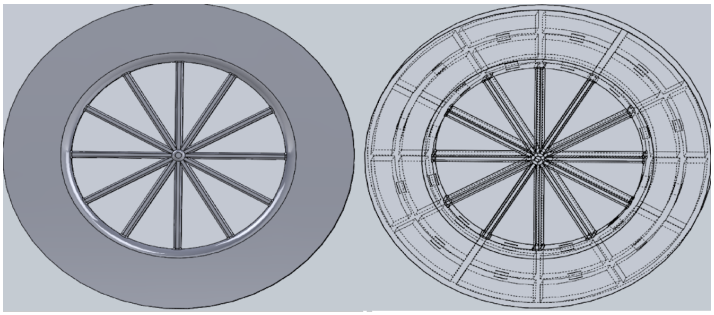

Figure 4.1: The first broadband design for an acoustic metamaterial.

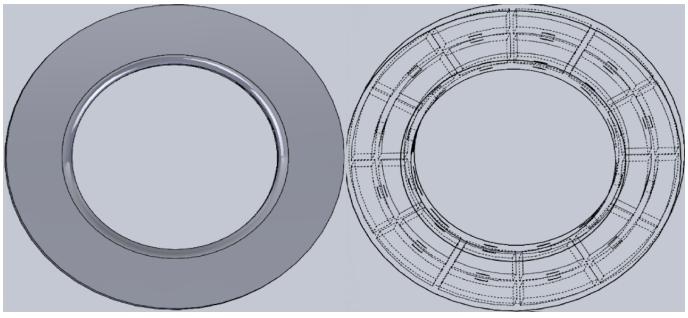

Figure 4.2: The second broadband design for an acoustic metamaterial.

The resonance frequency of the dual HR, measured in hertz, is given by:

$$f_{Dual\,HR} = \frac{c}{2\pi}\frac{\sqrt{\alpha_1}}{\sqrt{2}}\sqrt{1+\alpha_{21}(1+V_{21} \mp \sqrt{[1+\alpha_{21}(1+V_{21})]^2 - 4\alpha_{21}})} \tag{4.1}$$

where $\alpha_1 = \frac{A_{C1}}{l'_{C1}V_1}$, $\alpha_2 = \frac{A_{C2}}{l'_{C2}V_2}$, $\alpha_{21} = \frac{\alpha_2}{\alpha_1}$, $V_{21} = \frac{V_2}{V_1}$, A_{C1} is the cross-sectional area of the neck of the first HR, A_p is the cross-sectional area of the waveguide, l'_{C1} is the corrected neck length of the first HR, V_1 is the volume of the cavity of the first HR, and c is the speed of sound [27]. The resonance frequencies of the coupled HRs are shifted above and below the resonance frequency of the individual HR. This effect is due to pressure in both HRs either being in phase with each other or out of phase. The HRs in phase with each other act as one big resonator, which has a resonance below the resonance of the individual HR. The transmission loss for the dual HR, measured in dB, is given by:

$$TL\,(\omega) = 20\,log_{10}(1 + \frac{A_{C1}}{2A_p}\frac{1}{ikl'_{C1} + \frac{A_{C1}}{ik(\omega)V_1}(1 - \frac{A_{C2}V_2}{A_{C2}V_2 + A_{C2}V_1 - V_1V_2k(\omega)^2l'_{C2}})}) \tag{4.2}$$

where A_{C1} is the cross-sectional area of the neck of the first HR, A_p is the cross-sectional area of the waveguide, l'_{C1} is the corrected neck length of the first HR, V_1 is the volume of the cavity of the first HR, i is the imaginary number, and $k(\omega)$ is the wave number in terms of the angular frequency [27]. The transmission loss increases as the cross-sectional area of the waveguide decreases, which shows there is still a trade-off between transmission loss and airflow. The broadband sample design eliminates the obstacles to airflow found in the center of the previous designs by positioning the waveguides at the center of the sample. However, the trade-off for this design is weaker because the airflow loss starts at less than one percent with a minimum transmission loss of 9 dB. The transmission loss can be adjusted using the previous equation to be a minimum value across the bandwidth of the stop-band filter. This broadband design could be explored further to increase the transmission

loss while maintaining the low airflow loss.

REFERENCES

[1] Sofasco, "Sofasco dc fan series d6025-03 data sheet," Sofasco, Standard, May 2021. [Online]. Available: http://spingrfx.com/sofasco/pdf_files/d6025-03.pdf

[2] L. Kinsler, A. Frey, A. Coppens, and J. Sanders, *Fundamentals of Acoustics*. Wiley, 2000.

[3] D. Lee, D. M. Nguyen, and J. Rho, "Acoustic wave science realized by metamaterials," *Nano Convergence*, 2017. [Online]. Available: https://doi.org/10.1186/s40580-017-0097-y

[4] M. Yang and P. Sheng, "Sound absorption structures: From porous media to acoustic metamaterials," *Annual Review of Materials Research*, vol. 47, no. 1, pp. 83–114, 2017. [Online]. Available: https://doi.org/10.1146/annurev-matsci-070616-124032

[5] D. Raichel, *The Science and Applications of Acoustics*, ser. AIP series in modern acoustics and signal processing. Springer New York, 2006.

[6] D. Young, B. Munson, and T. Okiishi, *A Brief Introduction to Fluid Mechanics*. Wiley, 2003.

[7] F. White, *Fluid Mechanics*, ser. McGraw-Hill international editions. McGraw-Hill, 2003.

[8] T. Megson, *Structural and Stress Analysis*, ser. EngineeringPro collection. Elsevier Science, 2005.

[9] M. Biron, "7 - mechanical properties," in *Material Selection for Thermoplastic Parts*, M. Biron, Ed. Oxford: William Andrew Publishing, 2016, pp. 261 – 337. [Online]. Available: http://www.sciencedirect.com/science/article/pii/B9780702062841000076

[10] R. Daugherty, J. Franzini, and E. Finnemore, *Fluid Mechanics with Engineering Applications*. McGraw-Hill, 1985, no. v. 1.

[11] R. L. Panton and J. M. Miller, "Resonant frequencies of cylindrical helmholtz resonators," *The Journal of the Acoustical Society of America*, vol. 57, no. 6, pp. 1533–1535, 1975. [Online]. Available: https://doi.org/10.1121/1.380596

[12] T. A. Johansson and M. Kleiner, "Theory and experiments on the coupling of two helmholtz resonators," *The Journal of the Acoustical Society of America*, vol. 110, no. 3, pp. 1315–1328, 2001. [Online]. Available: https://doi.org/10.1121/1.1394741

[13] E. S. Menon, "Chapter 9 - series and parallel piping and power required," in *Pipeline Planning and Construction Field Manual*, E. S. Menon, Ed. Boston: Gulf Professional Publishing, 2011, pp. 177 – 204.

[14] Y. Cengel and J. Cimbala, *Fluid Mechanics Fundamentals and Applications: Third Edition*. McGraw-Hill Higher Education, 2013. [Online]. Available: https://books.google.com/books?id=QZIjAAAAQBAJ

[15] W. Forsthoffer, "2 - pump best practices," in *Forsthoffer's Best Practice Handbook for Rotating Machinery*, W. Forsthoffer, Ed. Boston: Butterworth-Heinemann, 2011, pp. 25 – 91.

[16] S. Moreau, M. Hennery, D. Casalino, J. Gullbrand, and G. Iaccarino. (2006) Toward the prediction of low-speed fan noise. [Online]. Available: https://web.stanford.edu/group/ctr/ctrsp06/moreau1_final.pdf

[17] J.-C. Cai, D.-T. Qi, and Y.-H. Zhang, "A Numerical Study of the Blade Passing Frequency Noise of a Centrifugal Fan," in *ASME International Mechanical Engineering Congress and Exposition*, vol. Volume 12: Vibration, Acoustics and Wave Propagation, 11 2012, pp. 335–343. [Online]. Available: https://doi.org/10.1115/IMECE2012-86745

[18] W. B. Cory, "15 - fan vibration," in *Fans and Ventilation*, W. B. Cory, Ed. Oxford: Elsevier Science, 2005, pp. 239 – 257. [Online]. Available: http://www.sciencedirect.com/science/article/pii/B9780080446264500176

[19] J.-C. Cai, Y. Zhang, and S. Long, "Computational estimation of fan casing noise at blade passing frequency component noise," *Applied Mechanics and Materials*, vol. 184-185, pp. 95–100, 06 2012.

[20] S.-H. Seo and Y.-H. Kim, "Silencer design by using array resonators for low-frequency band noise reduction," *The Journal of the Acoustical Society of America*, vol. 118, no. 4, pp. 2332–2338, 2005. [Online]. Available: https://doi.org/10.1121/1.2036222

[21] K. Mohapatra and D. P. Jena, "Benchmark analysis of a helmholtz resonator for estimating acoustic metamaterial properties," in *Advanced Materials*. Springer International Publishing, 2018, pp. 505–513.

[22] Standard test method for measurement of normal incidence sound transmission of acoustical materials based on the transfer matrix method. [Online]. Available: https://compass.astm.org/download/E2611-09.31043.pdf

[23] w, "A unique extraction of metamaterial parameters based on kramers kronig relationship," *Microwave Theory and Techniques, IEEE Transactions on*, vol. 58, pp. 2646–2653, 11 2010.

[24] C. Park and L. sang hun, "Zero-reflection acoustic metamaterial with a negative refractive index," *Scientific Reports*, vol. 9, 12 2019.

[25] D. Wu, N. Zhang, C. M. Mak, and C. Cai, "Hybrid noise control using multiple helmholtz resonator arrays," *Applied Acoustics*, vol. 143, pp. 31 –

37, 2019. [Online]. Available: http://www.sciencedirect.com/science/article/pii/S0003682X1830714X

[26] Bswa sw series impedance tube solutions. [Online]. Available: http://cdn.thomasnet.com/ccp/00370797/233605.pdf

[27] M. Xu, A. Selamet, and H. Kim, "Dual helmholtz resonator," *Applied Acoustics*, vol. 71, no. 9, pp. 822 – 829, 2010. [Online]. Available: http://www.sciencedirect.com/science/article/pii/S0003682X10000885